6 Seismic reflection and refraction

The seismic-reflection and -refraction methods in near-surface geophysical investigations are based on the introduction of mechanical energy into the subsurface using an active source and the recording, typically using surface geophones, of the resulting mechanical response. Passive-source seismic methods also provide important information; these will be described in Chapter 7. The propagation of mechanical energy into the subsurface consists, to a large part, of *elastic waves*. The essential property of an elastic body is that it returns instantaneously to its original pre-deformed state with the removal of a mechanical force that changed its size and/or shape. A delayed return to the original state is termed *viscoelasticity*. Any permanent deformation, such as ductile deformation or brittle failure, is a measure of the *inelasticity* of the body. Significant permanent deformation of the ground surface can occur in the vicinity of large seismic disturbances such as earthquakes (e.g. Lee and Shih, 2011) but inelasticity can be safely neglected in most near-surface active-source or passive-source studies. An important characteristic of elasticity is the relationship between the strain, or deformation, of a body and the stress, or mechanical force, that produces the deformation of the body. An excellent review of the elementary physics of wave motion is found in French (1971).

6.1 Introduction

There are several possible types of elastic wave motion following the introduction of a seismic disturbance. The particle motion associated with compressional, or P-waves, is aligned with the direction of wave propagation (Figure 6.1a). The particle motion associated with shear, or S-waves, is aligned in a direction perpendicular to the direction of wave propagation (Figure 6.1b). Both vertically polarized (SV, as shown in the figure) and horizontally polarized (SH) motions are possible. The P- and S-waves are known as *body waves* since they are transmitted through the interior of the Earth. As shown by the shaded cells in the figure, P-waves are associated with a change in size and aspect ratio of an elementary material volume while S-waves are associated with a change in shape. With surface Rayleigh, or R-waves, discussed more fully in the next chapter, the particle motion near the surface is retrograde elliptical (Figure 6.1c, top) and only those particles in the region close to the surface of the Earth, at depths comparable to the elastic wavelength, are set into motion. A second type of surface wave motion (Figure 6.1*c*, bottom) is characterized by horizontal particle motion that oscillates transverse to the direction of wave propagation. Such waves are termed Love waves.

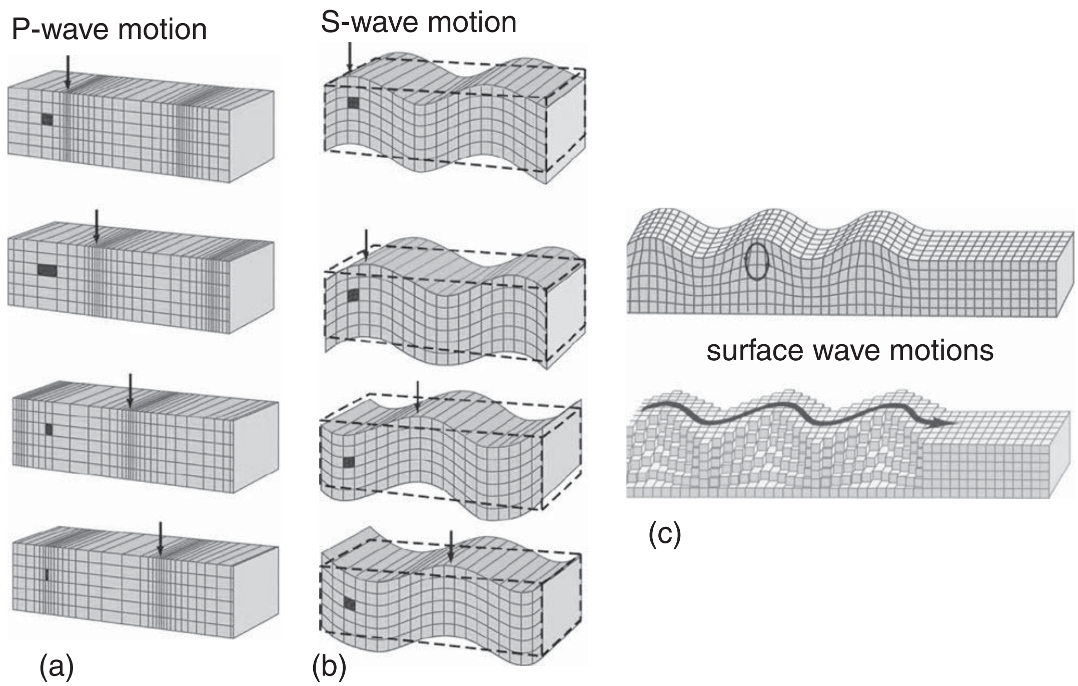

Figure 6.1 Particle motions associated with the propagation of seismic waves: (a) compressional; (b) shear (vertically polarized, SV); (c) two types of surface waves. Direction of propagation in all cases is to the right. After Grotzinger and Jordan (2010).

The following two case histories are presented to introduce the reader to recent applications of active-source seismology for imaging near-surface geological structures.

Example. High-resolution investigation for seismic hazard evaluation.

Reflection seismology offers a useful technique for seismic hazard assessment based on the study of buried fault structures. For example, in the New Madrid zone of contemporary seismicity within the northern Mississippi embayment of the central USA, neotectonic features are oftentimes obscured by Quaternary sediments. An integrated seismic-reflection analysis of P- and horizontally polarized SH-wave profiles was undertaken by Bexfield *et al.* (2006) to identify potentially reactivated Paleozoic bedrock faults that underlie the Quaternary cover. It is important to evaluate the extent of faulting in this area since critical facilities in this region such as dams, power plants, and bridges along the Ohio River are exposed to the significant intraplate earthquake hazard within the New Madrid seismic zone.

The P- and SH-wave profiles provide complementary perspectives on the subsurface at this location. The P-wave velocity responds strongly to the presence of water and the abundant methane gas since these fluids both affect the bulk modulus k. The SH-wave velocity, with its greater sensitivity to shear modulus μ, images primarily the solid rock or sediment component. The bulk and shear moduli, and their effect on seismic-wave propagation, are discussed later in this chapter. The SH-waves, despite a lower signal-to-noise ratio, yield higher spatial resolution in the uppermost 100 m since their wavelength is 0.3–0.5 times those of P-waves.

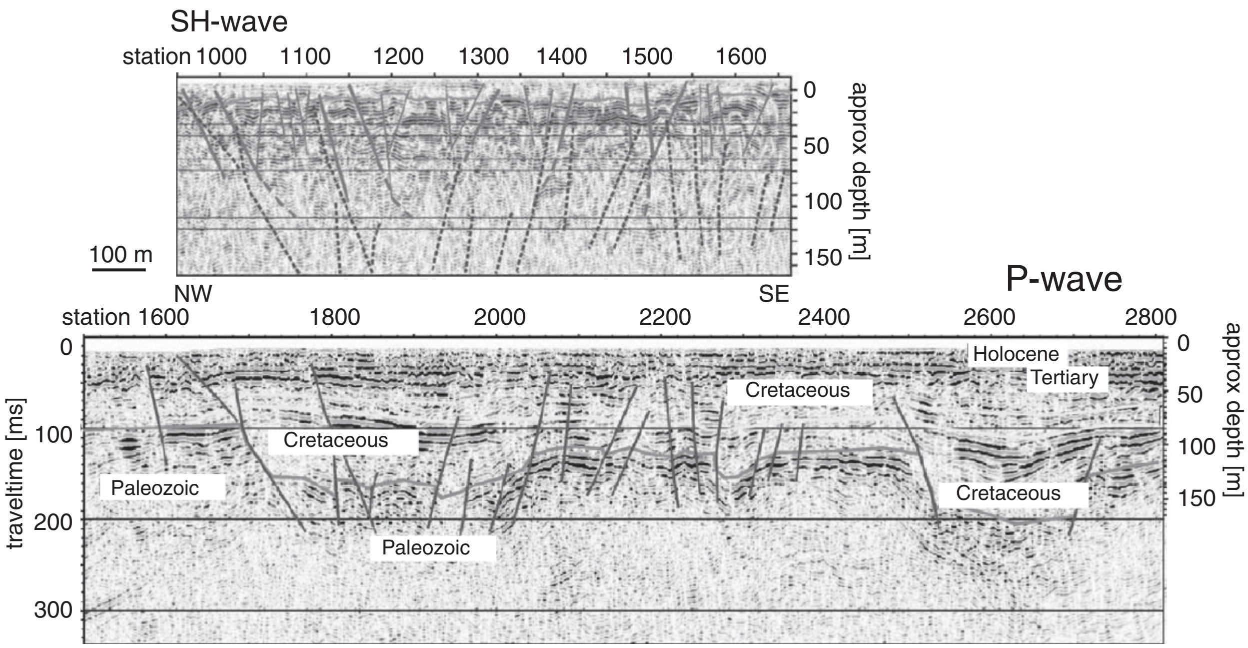

Figure 6.2 SH-wave (top) and P-wave (bottom) seismic profiles in the New Madrid zone of contemporary seismicity revealing reactivated Paleozoic bedrock normal faults. After Bexfield *et al*. (2006).

The seismic profiles shown in Figure 6.2 were acquired in wetlands adjacent to the Ohio River. Drilling in the region has indicated that depth to the Paleozoic bedrock is ~ 80–90 m beneath fluvial sediments and the underlying Paleocene to Cretaceous clay layers. The seismic P-wave section (Figure 6.2, bottom) reveals detailed images of bedrock faulting. Prominent in the profile, for example, are breaks in the bedrock reflector that are interpreted as grabens filled with Cretaceous sediments. The SH-wave section (Figure 6.2, top) does not clearly resolve to bedrock depths but does provide high-resolution images of near-surface deformation, including fine-scale faulting in the overlying Quaternary–Tertiary sediments. Many of the faults recognized in bedrock in the P-wave profile appear to propagate upward into the Quaternary sediments and are observed in the SH-wave profile.

Example. Shear-wave imaging of sinkholes in an urban environment.

Sinkholes in urban areas overlying karst or salt-dominated geology constitute another type of natural hazard. Human activities such as construction or groundwater utilization typically increase the potential for new sinkholes to develop or existing ones to re-activate. Krawczyk *et al*. (2011) describe the development of a shear-wave seismic imaging system that they have used to characterize active sinkholes in a built-up area of Hamburg, Germany. Although the cause of the sinkholes is not yet fully understood, they may be associated with dissolution of shallow salt and caprock structures. A major reason for concern is that microearthquake activity recently observed nearby may be a precursor to the imminent collapse of sinkholes.

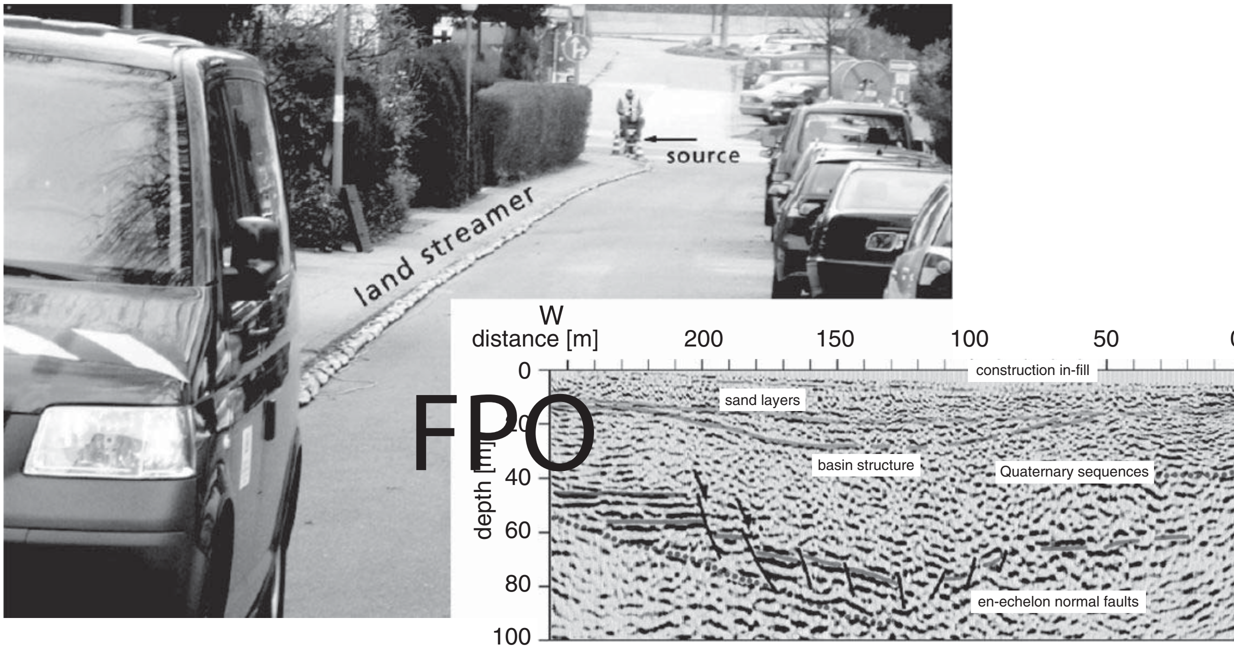

Figure 6.3 Shear-wave imaging of sinkholes in the city of Hamburg. After Krawczyk *et al*. (2011).

A 95-kg vibrator source swept through frequencies between 30 and 120 Hz was used to generate the shear waves. Signals were recorded using a land streamer of 120 geophones towed along a city street behind a vehicle (Figure 6.3, photo). The geophones were spaced 1 m apart and are preferentially sensitive to the detection of SH-polarized waves. The source spacing of 2.0 m resulted in ~ 40–50-fold data coverage (see the discussion on common midpoint profiling later in this chapter). The P-wave signals were largely suppressed by taking differences of traces acquired with opposite shear-wave polarity. After data processing, the migrated seismic section shown in Figure 6.3 was produced. The upper ~ 10 m of the section is interpreted as construction in-fill material and sandy layers. The basin-shaped seismic-reflecting horizon at 20–30 m depth observed within the Quaternary sedimentary sequence may be indicative of a subsidence feature. A pattern of en-echelon normal faults seen at ~ 55–80 m depths correlates with the known depth to the top of the salt/caprock structure. This case study demonstrates how seismic shear-wave analysis can be used for structural mapping in support of natural-hazard assessment in a noisy urban environment.

6.2 Stress and strain

An overview of the fundamental physics of elasticity is now presented. More complete, yet still elementary, treatments are given in Telford *et al*. (1990) and Gudmundsson (2011) while a more advanced approach may be found in Chapman (2004). The essential

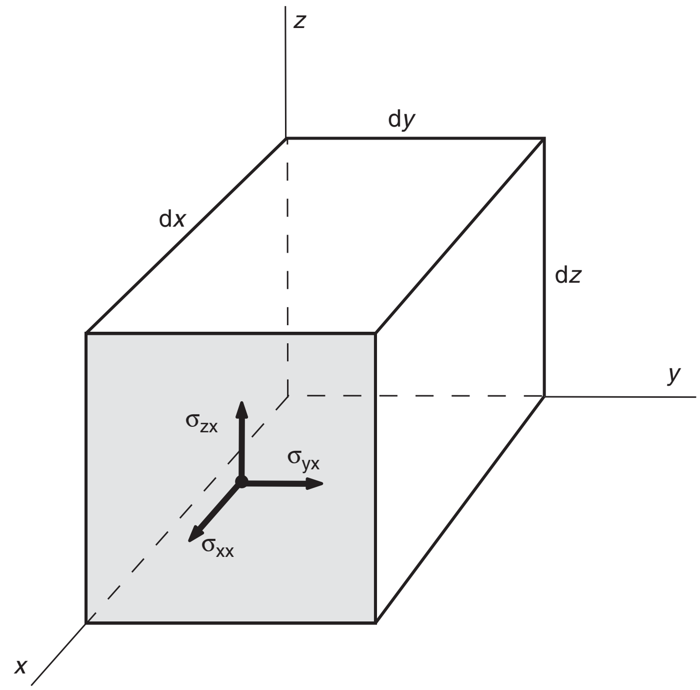

Figure 6.4 The three components of stress in a *yz*-plane perpendicular to the *x*-axis.

quantities in elasticity theory are stress and strain. Suppose a mechanical force is applied to an elastic body. Stress σ [Pa $=$ 1/Nm^2] is defined as the ratio of the applied force [N] to the area [m^2] over which the force acts. A normal stress, or *pressure*, occurs when the applied force is directed perpendicular to the area. The pressure is defined herein to be positive if the normal stress is tensile and negative if it is compressive. A *shear* stress, on the other hand, is directed tangential, or parallel, to the area over which it is applied. A arbitrary stress can be resolved into its normal and shear components. The three stress components (σ_{xx}, σ_{yx}, σ_{zx}) in the highlighted vertical plane perpendicular to the *x*-axis are shown in Figure 6.4. Note that σ_{xx} is a normal stress (shown here as tensile) while σ_{yx} and σ_{zx} are shear stresses.

Suppose the elastic body is in static equilibrium, so that it is not undergoing active deformation. In this case, the stresses must balance so that there is no net shear or pressure on the body. Accordingly, the three stress components (σ_{xx}, σ_{yx}, σ_{zx}) on the opposing *yz*-plane to the one highlighted in Figure 6.4 must be equal and opposite to the components shown in the figure. It must also be noted that the tangential stress components, such as σ_{yx} shown in the figure, exert a torque on the elastic body. An inspection of the figure indicates that, in order for the body to be in static equilibrium, the torque due to σ_{yx} must be counterbalanced by a stress component σ_{xy} of equal magnitude acting parallel to the *x*-axis in the *xz*-plane so that $\sigma_{yx=}$ σ_{xy}. In general, a condition for static equilibrium is a symmetric stress *tensor*, $\sigma_{ij} = \sigma_{ji}$, for $i, j = x, y, z$.

The small changes in size and shape that occur in response to stress are called strains. A simple rigid-body rotation through some angle θ or a rigid-body translation from one location to another, without a change in size and shape, does not constitute a strain. Strain ε is a dimensionless quantity defined as the fractional change in the size and shape of a body subject to loading. Suppose P and Q are two different points inside or on the surface of an elastic body. Let the vector $\mathbf{u}_P$ be the displacement of point P and the vector $\mathbf{u}_Q$ be the displacement of point Q in response to an applied stress. The strain is non-zero if $\mathbf{u}_P \neq \mathbf{u}_Q$ for any pair (P, Q). Strain can also be decomposed into normal and shear components.

Let the three Cartesian components of the displacement vector be denoted as $\mathbf{u} = (u, v, w)$. The diagonal element ε_{ii} of the strain tensor is the relative increase in length along the i-axis, where $i = x, y, z$, such that

$$\varepsilon_{xx} = \frac{\partial u}{\partial x}; \ \varepsilon_{yy} = \frac{\partial v}{\partial y}; \ \varepsilon_{zz} = \frac{\partial w}{\partial z}. \tag{6.1}$$

The *dilatation* Δ of a body is its fractional change in volume, given by

$$\Delta = \varepsilon_{xx} + \varepsilon_{yy} + \varepsilon_{zz} = \frac{\partial u}{\partial x} + \frac{\partial v}{\partial y} + \frac{\partial w}{\partial z}. \tag{6.2}$$

The diagonal elements of the strain tensor are normal strains and they describe the change in size of the body. The shear strains are the off-diagonal elements of the strain tensor that describe a change in shape of the body. The shear strains are defined as

$$\varepsilon_{xy} = \varepsilon_{yx} = \frac{\partial v}{\partial x} + \frac{\partial u}{\partial y}; \tag{6.3a}$$

$$\varepsilon_{yz} = \varepsilon_{zy} = \frac{\partial w}{\partial y} + \frac{\partial v}{\partial z}; \tag{6.3b}$$

$$\varepsilon_{zx} = \varepsilon_{xz} = \frac{\partial u}{\partial z} + \frac{\partial w}{\partial x}. \tag{6.3c}$$

For the very small strains that are relevant to near-surface seismology, a useful idealized description of the relationship between stress and strain is provided by *Hooke's law*. The law states that a given strain is directly proportional to the stress producing it and, moreover, the strain occurs simultaneously with application of the stress. A principle of superposition also applies: when several stresses are present, each stress produces a strain independently of the others. In an isotropic medium, in which elastic properties do not depend on direction, Hooke's law for normal and shear stresses is written as

$$\sigma_{ii} = \lambda\Delta + 2\mu\varepsilon_{ii}, \text{for } i = x, y, z; \tag{6.4a}$$

$$\sigma_{ij} = \mu\varepsilon_{ij}, \text{for } i \neq j; \tag{6.4b}$$

with $\lambda > 0$. The quantities (λ, μ) are known as the Lamé parameters. The parameter μ, as shown by equation (6.4b), determines the amount of shear strain that develops in response to a given applied shear stress. The parameter μ accordingly is termed the *shear modulus*. For liquids, which offer no resistance to shearing forces, the strain is unbounded and $\mu = 0$.

The Lamé parameter λ is not often used in applied geophysics. Of more practical importance is the *bulk modulus* k

$$k = \frac{3\lambda + 2\mu}{3}, \tag{6.5}$$

which provides a measure of the resistance of a material to a uniform compressive stress.

Table 6.1 Bulk and shear moduli of common geomaterials

	Bulk modulus, k [N/m^2]	Shear modulus, μ [N/m^2]
Limestone	3.7–5.7	2.1–3.0
Granite	2.7–3.3	1.5–2.4
Sandstone	1.25	0.6

Table 6.1 gives values of shear and bulk moduli for common geomaterials. More extensive tables of elastic moduli appear throughout the geophysical literature.

6.3 Wave motion

An elastic body will not remain in static equilibrium if it is acted upon by unbalanced stresses. Suppose for example that the stress on the back face of the cube in Figure 6.4 is σ_{xx} while the stress on the front face is slightly different, $\sigma_{xx}+(\partial\sigma_{xx}/\partial x)\mathrm{d}x$. Suppose similar expressions hold for stresses in other directions. The mass of the cube is $\mathrm{d}m = \rho \mathrm{d}x\mathrm{d}y\mathrm{d}z$, where ρ [kg/m^3] is the density. To determine the motion caused by the unbalanced stresses, an infinitesimal version of Newton's familiar law $\mathbf{F} = m\mathbf{a}$ applies; for example, the x-component of the force law is

$$\rho \frac{\partial^2 u}{\partial t^2} = \frac{\partial \sigma_{xx}}{\partial x} + \frac{\partial \sigma_{xy}}{\partial y} + \frac{\partial \sigma_{xz}}{\partial z}. \tag{6.6}$$

We can now use Hooke's law and the definition of the strain tensor to re-write Equation (6.6) purely in terms of the displacement u as

$$\rho \frac{\partial^2 u}{\partial t^2} = (\lambda + \mu) \frac{\partial \Delta}{\partial x} + \mu \Delta^2 u, \tag{6.7a}$$

where $\Delta^2 = \partial^2/\partial x^2 + \partial^2/\partial y^2 + \partial^2/\partial z^2$ is the Laplacian operator and Δ is the dilatation defined in Equation (6.2). Similar equations are satisfied by v and w, i.e. the displacements in the y and z directions, respectively. These are

$$\rho \frac{\partial^2 v}{\partial t^2} = (\lambda + \mu) \frac{\partial \Delta}{\partial y} + \mu \Delta^2 v, \tag{6.7b}$$

$$\rho \frac{\partial^2 w}{\partial t^2} = (\lambda + \mu) \frac{\partial \Delta}{\partial z} + \mu \Delta^2 w. \tag{6.7c}$$

Now, differentiate the above three expressions with respect to x, y, and z respectively and add the results together. This procedure gives

$$\rho \frac{\partial^2 \Delta}{\partial t^2} = (\lambda + 2\mu) \nabla^2 \Delta, \tag{6.8}$$

which we immediately recognize as the familiar wave equation

$$\frac{1}{V_P^2}\frac{\partial^2 \Delta}{\partial t^2} = \nabla^2 \Delta \tag{6.9}$$

where $V_P = \sqrt{(\lambda + 2\mu)/\rho}$ is the wave velocity. The associated waves are called dilatational, compressional, or *P*-waves, and V_P is the *P*-wave velocity.

A second set of wave equations may be derived as follows. Subtracting the *z*-derivative of Equation (6.7b) from the *y*-derivative of Equation (6.7c) yields

$$\rho \frac{\partial^2}{\partial t^2}\left(\frac{\partial w}{\partial y} - \frac{\partial v}{\partial z}\right) = \mu \nabla^2 \left(\frac{\partial w}{\partial y} - \frac{\partial v}{\partial z}\right). \tag{6.10}$$

If we define the rotational parameter $\theta_x = \partial w/\partial y - \partial v/\partial z$ then Equation (6.10) simplifies to the wave equation

$$\frac{1}{V_S^2}\frac{\partial^2 \theta_x}{\partial t^2} = \nabla^2 \theta_x \tag{6.11}$$

with the wave velocity $V_S = \sqrt{\mu/\rho}$. There are two other wave equations for θ_y and θ_z, respectively. The waves are called rotational, shear, or *S*-waves, and V_S is the *S*-wave velocity. Notice that the *P*-wave velocity always exceeds the *S*-wave velocity, $V_P > V_S$. The *S*-wave velocity is normally about 40–60% but never exceeds about 70% of the *P*-wave velocity. Physically, V_P is larger than V_S since solid materials generally offer greater resistance to the imposition of compressive forces as opposed to shearing forces.

Near-surface geophysicists routinely use P-waves. As we have already seen, some studies use shear waves but special sources, receivers, and acquisition and processing procedures are required to cancel the P-waves. In reflection or refraction studies, surface Rayleigh R-waves are generally considered as a source of noise, known as *ground roll*, but as shown in the next chapter important information can often be extracted from their analysis and, less frequently, from the analysis of Love waves. A fourth type of seismic wave is a guided wave, or *Lamb wave*. This wave is confined to subsurface thin layers and is sometimes useful for probing underground features such as coal seams, fault zones, and subsurface voids.

6.4 Seismic waves and elastic moduli

It is worthwhile to look briefly at relationships between the seismic wave velocities V_P and V_S and the elastic moduli. These relationships are of great interest to geotechnical engineers and others who require a knowledge of spatially distributed soil mechanical properties. Young's modulus E [N/m^2] is a measure of the longitudinal stress to the longitudinal strain (see Figure 6.5a); roughly speaking, high values of E indicate a stiff material while smaller values indicate a compliant, or soft material. Poisson's ratio σ is a dimensionless measure of the transverse strain to longitudinal strain (Figure 6.5b). The formulas are

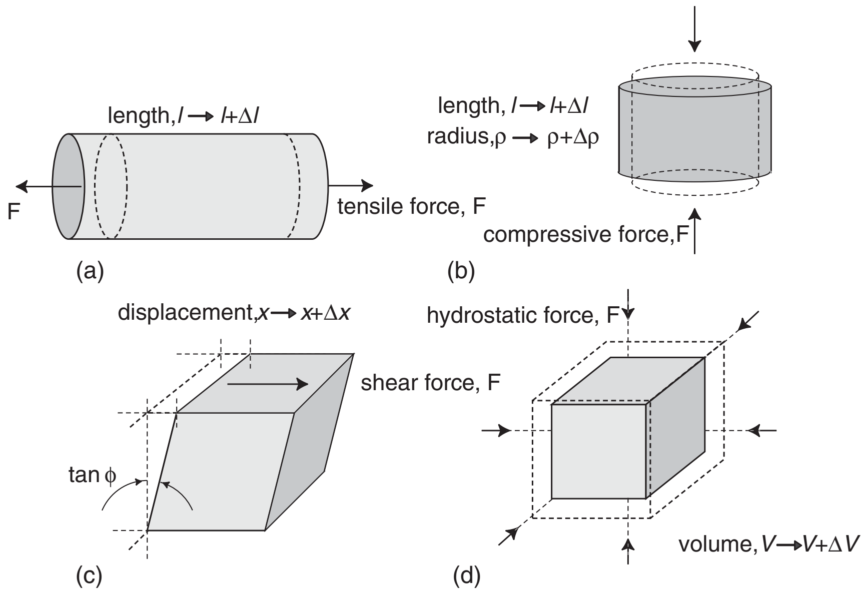

Figure 6.5 Definitions of the elastic moduli: (a) Young's modulus E; (b) Poisson's ratio σ; (c) shear modulus μ; and (d) bulk modulus k.

$$E = \frac{F/A}{\Delta l/l} = \frac{\mu(3\lambda + 2\mu)}{\lambda + \mu}; \tag{6.12}$$

$$\sigma = \frac{\Delta\rho/\rho}{\Delta l/l} = \frac{\lambda}{2(\lambda + \mu)}. \tag{6.13}$$

As mentioned earlier, the shear modulus μ [N/m^2] is a measure of the tangential stress to tangential strain, or shear stiffness, while the bulk modulus k [N/m^2] is a measure of the volume change in response to a change in hydrostatic pressure, or compressibility; see Figure 6.5c, d. The formulas are

$$\mu = \frac{F/A}{\tan\varphi}; \tag{6.14}$$

$$k = \frac{F/A}{\Delta V/V} = \frac{3\lambda + 2\mu}{3}. \tag{6.15}$$

Relationships amongst the seismic velocities and the elastic moduli are

$$V_P = \sqrt{\frac{k + 4\mu/3}{\rho}} = \sqrt{\frac{(1-\sigma)E}{(1+\sigma)(1-2\sigma)\rho}}; \tag{6.16}$$

$$V_S = \sqrt{\frac{\mu}{\rho}} = \sqrt{\frac{E}{2\rho(1+\sigma)}}; \tag{6.17}$$

where ρ is the density of the medium. It is important to note that both seismic velocities V_P and V_S are observed to increase with increasing density, even though it appears from Equations (6.16) and (6.17) that inverse relationships of the form $V \sim 1/\sqrt{\rho}$ exist.

The explanation is that the numerators $k + 4\mu/3$ and μ increase with increasing ρ faster than $1/\rho$ decreases.

Certain tasks in geotechnical engineering, including the design of bridge and building foundations, require a knowledge of the shear strength of the subsurface soil and rock. Determining an accurate value for the Poisson's ratio σ is fundamentally important in such studies. Poisson's ratio ranges from $\sigma \sim 0.3$ in competent sandstone and limestone to $\sigma \sim 0.45$ in unconsolidated sediments. From Equations (6.16) and (6.17) we find

$$\frac{V_P}{V_S} = \sqrt{\frac{2(1-\sigma)}{1-2\sigma}}; \tag{6.18}$$

thus it is evident that Poisson's ratio can be estimated *in situ* from a seismic determination of the velocities V_P and V_S. Near-surface applied geophysics is shown by this example to be directly relevant and useful to geotechnical engineers.

6.5 Seismic velocity of geomaterials

As shown in the previous section, the theory of elasticity indicates that the seismic velocities V_P and V_S of a homogeneous medium depend on density ρ and the elastic moduli, k and μ, according to Equations (6.16) and (6.17). However, in many practical situations, it is of interest to determine the bulk seismic velocities of mixtures of geomaterials such as fluid-bearing or clay-bearing sediments and consolidated rocks.

The *Nafe–Drake* curve is an empirical relationship between the P-wave velocity and density of water-saturated marine sediments that has been widely used for many years in exploration and crustal-scale geophysics (see e.g. Fowler, 2005, p.103). Wyllie's mixing law (Wyllie *et al*., 1958),

$$\frac{1}{V_{bulk}} = \frac{\phi}{V_{fluid}} + \frac{1-\phi}{V_{solid}}, \tag{6.19}$$

is used extensively in well log analysis, where ϕ is porosity. It expresses the seismic P-wave traveltime ($\sim 1/V_{bulk}$) in a fluid-saturated medium as the porosity-weighted average of the P-wave traveltimes in the fluid and solid constituents, $\sim 1/V_{fluid}$ and $\sim 1/V_{solid}$, respectively. Other mixing laws have been proposed in the literature to explain velocity–porosity relations, with velocity generally falling as porosity increases. A good review of the literature on the bulk seismic velocities of various mixtures of geomaterials is given by Knight and Endres (2005).

Marion *et al*. (1992) have measured the seismic velocity of water – -saturated, unconsolidated sand–clay mixtures. They find that bulk V_P peaks at a critical value of the clay content, roughly 40%. The following explanation for this behavior is offered. In shaly sands (clay content less than critical value), sand is the load-bearing element and the clay particles are dispersed in the pore space between the sand grains. Increasing the

Table 6.2 Seismic compressional wave velocities

	Velocity [m/s]		Velocity [m/s]
Air	330	Sandstone	1500–4500
Sand (dry)	200–800	Ice	3000–4000
Clay	1100–2500	Limestone	2500–6500
Sand (saturated)	800–1900	Granite	3600–7000
Water	1450	Basalt	5000–8400

clay content of shaly sands fills in the pore space, thereby decreasing the bulk porosity while stiffening the pore-filling material. Both these effects tend to increase the bulk velocity. In sandy shales (clay content higher than critical value), the sand grains are suspended in a clay matrix. In this regime, increasing further the clay content increases the bulk porosity of the mixture since the porosity of pure clay is higher than that of pure sand. This increase in bulk porosity causes the velocity in sandy shales to decrease. Right at the critical value, there is just enough clay to completely fill the space between sand grains. This configuration is the one of minimum bulk porosity, and hence the observed peak in seismic velocity. The work of Marion *et al*. (1992) applies to unconsolidated sand–clay mixtures. Gal *et al*. (1999) point out that, in consolidated sandstones, clay can act as a load-bearing element by coating the sand grains and cementing them together. In such cases, V_P increases rapidly and monotonically with increasing clay content.

A rough guide to the P-wave velocities of selected geomaterials is shown in Table 6.2. The wide ranges in velocities are due in part to variations in lithology, but more important in near-surface geophysics are the general rules that unsaturated, unconsolidated, weathered, fractured, unfrozen, and heterogeneous geomaterials have lower seismic velocities than their saturated, consolidated, unweathered, intact, frozen, and homogeneous counterparts. In the near-surface zone of aeration, bulk seismic velocity is often less than that of water and can become less than that of air. In anisotropic media such as finely interbedded sediments or fractured rocks, the velocity parallel to the strike direction is typically greater by 10–15% than the velocity across the strike.

The effect on seismic velocities of dense non-aqueous-phase liquid (DNAPL) contamination has been examined in the laboratory by Ajo-Franklin *et al*. (2007). They find that bulk V_P of both natural sandy aquifer and synthetic glass-bead samples is reduced by up to ~ 15% as trichloroethylene (TCE) saturation increases to ~ 60%. Such high TCE concentrations have been found at actual contaminated sites but the spatial extent of the accumulations are typically far below the spatial resolution of seismic experiments.

For S-waves, Santamarina *et al*. (2005) quote a range of V_S from less than 50 m/s up to 400 m/s for near-surface saturated soils, rising to 250–700 m/s for lightly cemented soils.

6.6 Reflection and refraction at an interface

The behavior of a seismic wave incident upon an interface between two elastic media is shown in Figure 6.6. One part of the wave energy is *reflected* back into medium 1 while another part is *refracted* into medium 2. Elastic waves are distinguished from optical or acoustic waves in the sense that an incident compressional wave is split into both compressional and shear reflected and refracted components, a process termed P-to-S conversion.

The laws of reflection and refraction may be derived using Huygen's principle. This principle is helpful to understanding the time evolution of seismic *wavefronts*. A wavefront is a surface on which all particles are in the same phase of motion. Huygen's principle states that every point along a wavefront can be regarded as a new source of waves. The future location of a wavefront can therefore be determined by propagating a spherical wavelet from each point on the current wavefront. As shown in Figure 6.7, let AB be the seismic wavefront at time t_0. After some time interval Δt, the wave will have advanced a distance $V\Delta t$, as shown. Centered on each sampled point on the current waveform we draw arcs of radius $V\Delta t$. The new wavefront $A'B'$ is simply the envelope of these arcs, as indicated in the figure. The accuracy of the wavefront construction increases as we draw arcs from a finer sampling of points on the current waveform.

Consider now a planar wavefront AB incident upon a plane interface between two materials with P-wave velocities V_1 and V_2, respectively, as shown in Figure 6.8. When the point A arrives at the interface, the wavefront is labeled as $A'B'$. Point B', at this time, is at distance $V_1\Delta t$ from the interface. During the time interval Δt that it takes for B' to reach point R on the interface, part of the energy at A' would have traveled the same distance

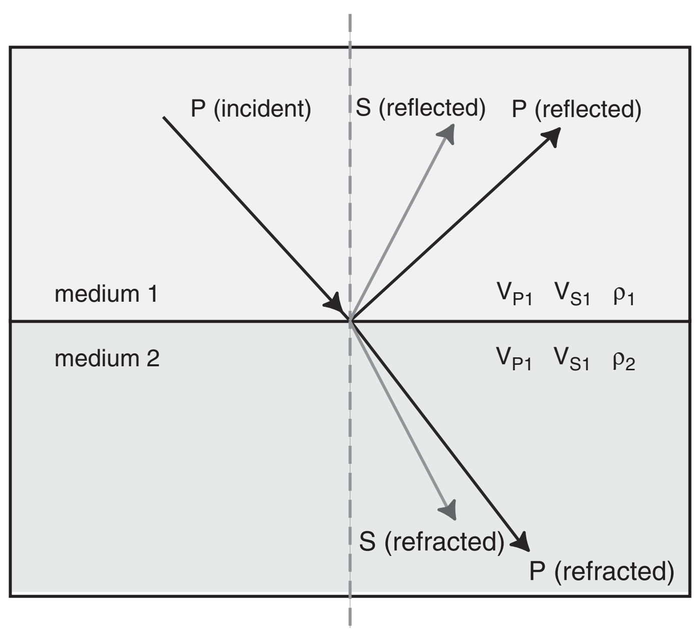

Figure 6.6 P-wave reflection and refraction at an interface, including P-to-S conversion.

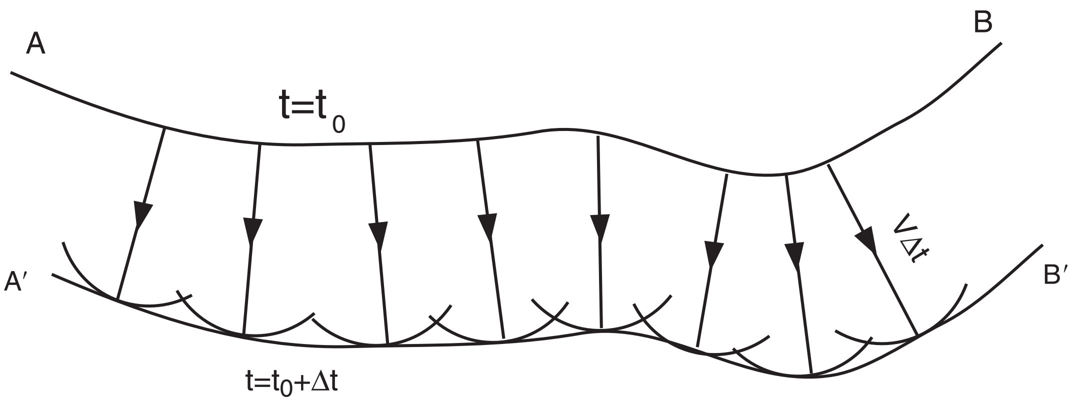

Figure 6.7 Wavefront construction based on Huygen's principle.

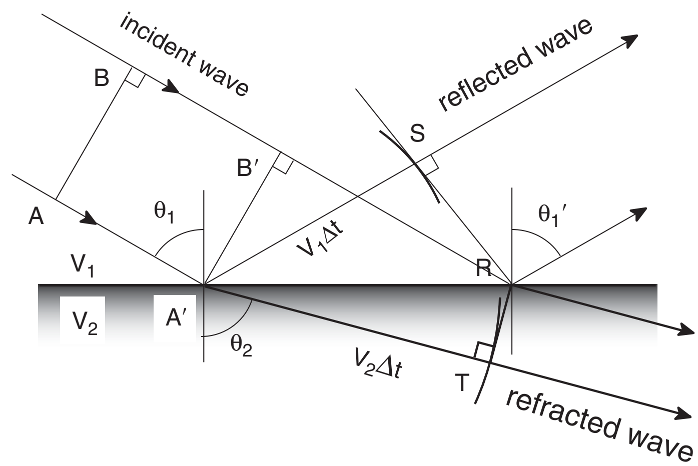

Figure 6.8 Reflection and refraction of a plane wave.

$V_1\Delta t$ upward back into original medium, while the remainder would have refracted a distance $V_2\Delta t$ into the underlying medium.

To determine the angles of reflection and refraction, we can use Huygen's principle. Accordingly, arcs are drawn with center A' and radii $V_1\Delta t$ and $V_2\Delta t$. The new wavefronts, denoted RS and RT are constructed by drawing tangents to these arcs that intersect point R. A glance at the geometry of the figure shows that the angle of incidence θ_1 is equal to the angle of reflection $\theta_1{}'$; this is the *law of reflection*. Another glance at the figure shows that $V_1\Delta t = A'R \sin\theta_1$ and $V_2\Delta t = A'R \sin\theta_2$. Solving both equations for the quantity $A'R/\Delta t$ gives

$$\frac{\sin\theta_1}{V_1} = \frac{\sin\theta_2}{V_2} = p; \tag{6.20}$$

which is the familiar *Snell's law of refraction*. The quantity p in Equation (6.20) is termed the *ray parameter*. If the medium consists of a number of parallel layers, the ray parameter p does not change from its initial value in the first layer as the wave refracts through the

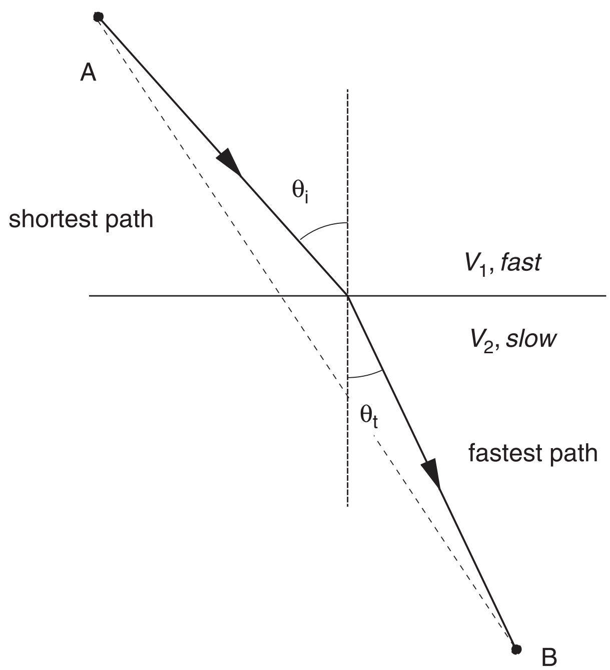

Figure 6.9 Fermat's principle of least time.

stack of layers. An equivalent derivation of the laws of reflection and refraction using Fermat's *principle of least time* (see Figure 6.9), rather than Huygen's principle, is left as an exercise at the end of the chapter.

If a P-wave is incident on an interface, it should be noted that the angles of refraction for both the P-wave and the S-wave can be found by Snell's law using the appropriate P-wave and S-wave velocities in Equation (6.20). Since $V_{P2} > V_{S2}$, it follows that $\sin\theta_{P2} > \sin\theta_{S2}$. Accordingly, as shown in Figure 6.6, the direction of the refracted S-wave is closer to the vertical than that of the refracted P-wave. Similarly, the angle of reflection θ'_{S1} of the S-wave for an incident P-wave may be found from a generalized law of reflection, $\sin\theta'_{P1}/V_{P1} = \sin\theta'_{S1}/V_{S1}$.

For P-waves incident on a low-velocity layer in which $V_2 < V_1$, Snell's law predicts that $\theta_2 < \theta_1$ and thus the wave refracts downward, toward the normal to the interface. Suppose, instead, that the wave is incident on a relatively fast layer in which $V_2 > V_1$. The wave refracts toward the horizontal interface. It is possible to observe an angle of refraction $\theta_2 = 90°$ for the case that the incident angle happens to be $\theta_1 = \sin^{-1}(V_1/V_2)$. The refracted wave in this case travels along the interface between the two media. This is the critically refracted wave and $\theta_C = \sin^{-1}(V_1/V_2)$ is called the *critical angle*. For angles of incidence that are greater than the critical angle, $\theta_1 > \theta_C$, no refraction occurs and there is *total internal reflection* of all the wave energy back into the original medium.

The law of reflection and Snell's law of refraction provide the directions of propagation of the reflected and the refracted waves, but they do not allow us to calculate the relative amplitudes of these waves. The partitioning of energy into the reflected and refracted body waves is described by the Zoeppritz equations (Shuey, 1985). A complete derivation of these equations, which is not undertaken here, requires to solve the elastic wave equation subject to conditions that the normal and tangential components of stress and displacement are continuous across the interface. A detailed calculation reveals that the reflection and refraction coefficients (R, T) depend in a somewhat complicated fashion on the angle of incidence, but for P-waves at normal incidence they reduce to

$$R = \frac{\rho_2 V_2 - \rho_1 V_1}{\rho_2 V_2 + \rho_1 V_1}; \tag{6.21}$$

$$T = \frac{2\rho_1 V_1}{\rho_2 V_2 + \rho_1 V_1}; \tag{6.22}$$

where (ρ_1, ρ_2) are the densities and (V_1, V_2) are the wave velocities of the two media. The reflection coefficient generally obeys $R < 0.2$ for stratification within unconsolidated near-surface geomaterials. The energy reflected at such interfaces is proportional to the square of the wave amplitude and hence $R^2 < 4\%$. Thus, very little of the energy transmitted into the ground by the seismic source is reflected back to the surface where it may be recorded by geophones. On the other hand, the top of competent bedrock (say, $V_P \sim 4500$ km/s) lying below unconsolidated sediments (say, $V_P \sim 800$ km/s) reflects almost 60% of the normally incident seismic wave energy. The Zoeppritz equations further reveal that most of the incident energy is partitioned into reflected and refracted P-waves and only a minor amount is partitioned into reflected and refracted S-waves.

The product ρV that appears in Equations (6.21) and (6.22) is termed the *acoustic impedance*. It is often stated that the seismic-reflection method provides images of subsurface discontinuities in acoustic impedance.

6.7 Diffraction

Seismic energy is *diffracted* if a wave encounters a subsurface feature whose radius of curvature is smaller or not significantly larger than the seismic wavelength, $\lambda = V/f$. Seismic wavelengths are large (e.g. $\lambda = 5.0$ m for $V = 1.5$ km/s and $f = 300$ Hz; typical values encountered in practice) so that understanding diffraction effects is very important in near-surface seismic interpretation. While a rigorous theoretical description of diffraction is beyond the scope of this book, to first order a diffracted wavefront can be constructed using Huygen's principle.

Consider a vertically propagating seismic plane wave that is incident on a sedimentary bed that pinches out, forming a type of wedge, as shown in Figure 6.10. The energy contained in the part of the wavefront that strikes the tip of the wedge scatters in all directions (Keller, 1957). In essence, the wedge tip acts as a point scatterer, or *diffractor*. As shown in the figure, diffracted seismic energy also propagates beneath the wedge.

6.8 Analysis of idealized reflection seismograms

A simplified analysis of seismic-wave propagation uses *rays*, which are semi-infinite lines oriented perpendicular to wavefronts and pointing in the direction of wave propagation. A ray changes direction if the propagating wavefront encounters a change in acoustic impedance. *Ray paths* are used to indicate the various routes of wave propagation between a

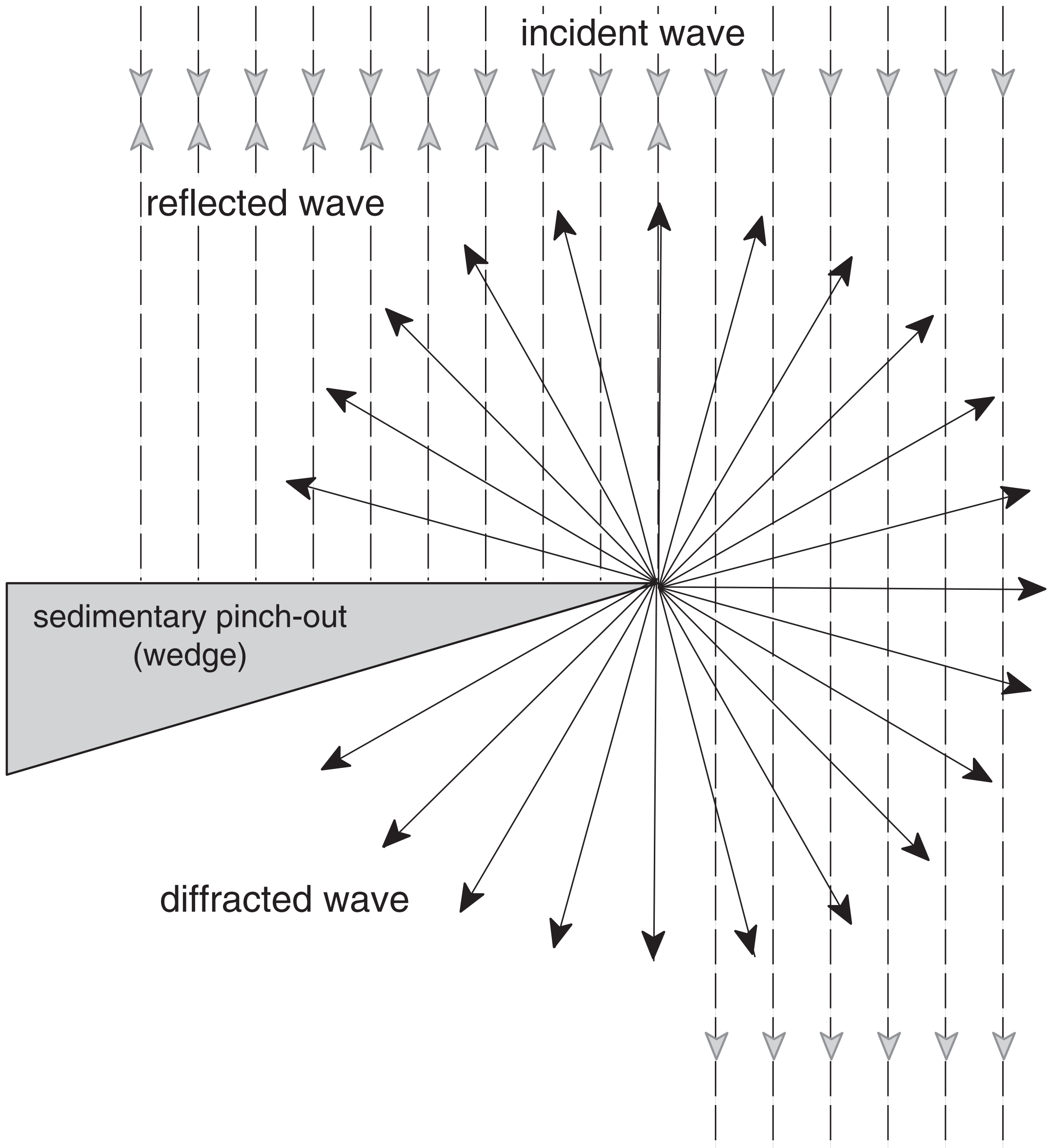

Figure 6.10 Diffraction by a wedge.

seismic source (transmitter, TX) and a geophone (receiver, RX). There are three important ray paths in the simple one-layer scenario shown in Figure 6.11. These paths trace the fastest routes of direct, reflected, and refracted seismic energy from TX to RX and hence they satisfy Fermat's principle of least time. It proves insightful to analyze the traveltime of the *P*-waves along these paths. Let x be the TX–RX separation distance. The direct *P*-wave traveltime along path 1 is very simply given by the distance divided by the velocity, $\tau_1(x) = x/V_1$.

The traveltime $\tau_2(x)$ for the primary *P*-wave reflection, shown as path 2 in Figure 6.11, is given by

$$\tau_2(x) = \frac{2}{V_1}\sqrt{h^2 + \left(\frac{x}{2}\right)^2}, \tag{6.23}$$

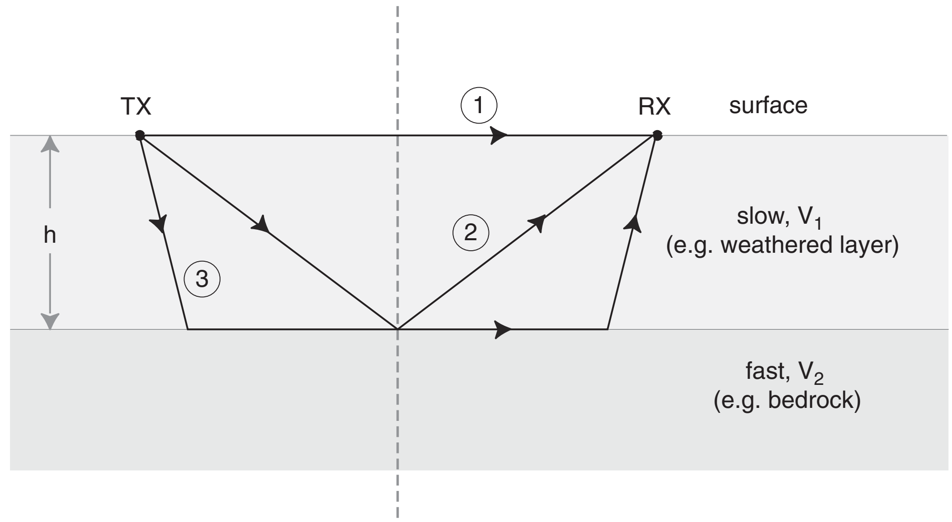

Figure 6.11 Important ray paths between seismic source (TX) and geophone (RX): (1) direct *P*-wave; (2) reflected *P*-wave; (3) refracted *P*-wave.

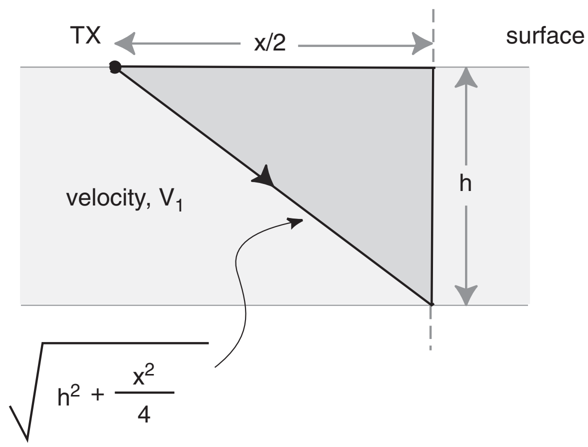

Figure 6.12 Geometry associated with the primary *P*-wave reflection.

where the $h^2 + (x/2)^2$ term corresponds to the slant distance shown in Figure 6.12.

The square of the traveltime Equation (6.23), given by

$$\tau_2^2(x) = \tau_0^2(x) + \frac{x^2}{V_1^2}, \tag{6.24}$$

describes a hyperbola with intercept (or zero-offset traveltime) $\tau_0 = 2h/V_1$. The hyperbolic increase in traveltime τ_2 with increasing TX–RX offset x is called the *normal moveout*. An idealized seismogram showing a P-wave reflection is shown in Figure 6.13. The hyperbolic curve in the figure has been computed using the values $h = 1.0$ m and $V_1 = 1500$ m/s. Each vertical trace in the seismogram corresponds to a single geophone response. The collection of traces, displayed in this manner, is termed a *shot gather*.

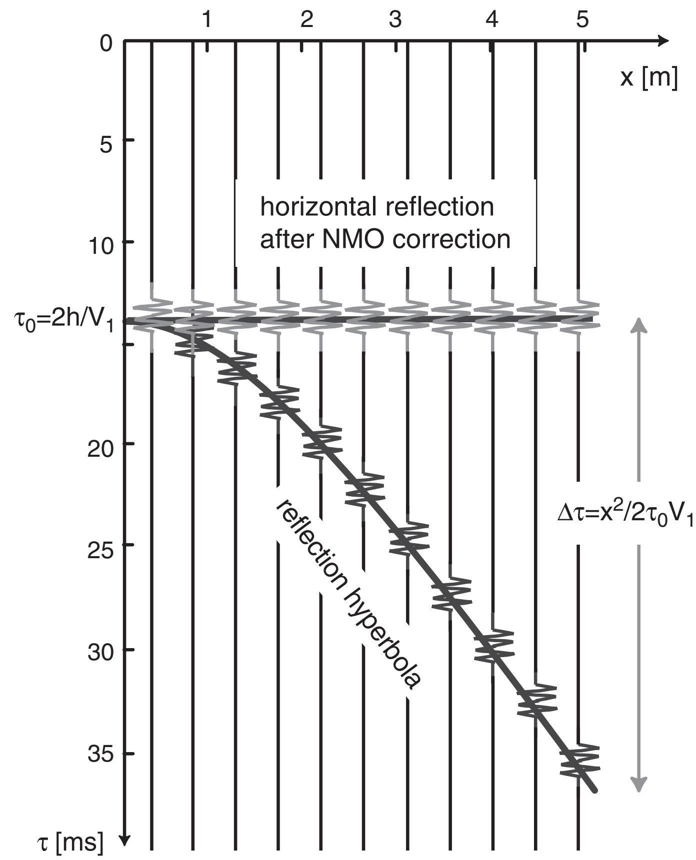

Figure 6.13 Idealized seismogram (shot gather) of primary *P*-wave reflection showing hyperbolic moveout curve and NMO-corrected horizontal reflector.

A plot of τ_2^2 vs x^2 would give a slope of $1/V_1^2$, according to Equation (6.24), and an intercept of $\tau_0^2 = 4h^2/V_1^2$. Thus, an analysis of the slope and intercept of the τ_2^2 vs x^2 plot enables a determination of the layer thickness h and the layer velocity V_1.

Notice that the idealized seismogram, with its hyperbolic *P*-wave reflection event, does not display an accurate image of the subhorizontal velocity contrast between the slow weathered layer and the fast bedrock shown in Figure 6.11. The apparent curvature of the subsurface reflector is due to the variable distance x between the TX and each RX in the geophone array. The subhorizontal velocity contrast would have been accurately imaged if, however, each seismic trace was due to a separate TX located in the same position as each geophone. This hypothetical TX–RX configuration is termed the zero-offset data-acquisition geometry.

A normal moveout (NMO) correction can be applied to each seismic trace. This procedure converts the seismogram into one that would have been measured for zero-offset acquisition across the geophone array. The NMO correction has the effect of straightening out the hyperbolic moveout curves and thereby providing an accurate image of the subhorizontal reflector (see Figure 6.13). Notice that the reflector at the left-most seismic trace (close to zero TX–RX offset, $x = 0$) is already very nearly in its correct position. Multiples, and any other events that have reflected from more than one interface within the subsurface, do not exhibit a normal moveout.

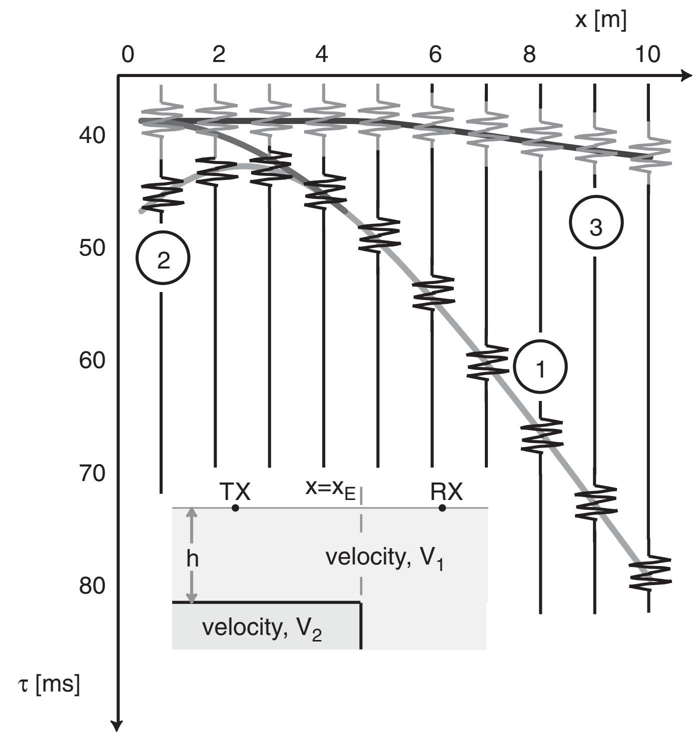

Figure 6.14 Idealized seismogram showing: (1) primary P-wave reflection; (2) diffracted wave from the edge shown in the insert; and (3) the standard NMO-corrected arrivals. For these calculations, $h = 3.0$ m; $V_1 = 1500$ m/s, and location of the edge, $x_E = 2.0$ m.

It is clear from an inspection of the idealized seismogram that the NMO correction $\Delta\tau$ to each seismic trace should be

$$\Delta\tau(x) = \tau_2(x) - \tau_0 \tag{6.25}$$

since the reflection hyperbola is $\tau_2(x)$ and the zero-offset two-way traveltime is τ_0.

Applying an NMO correction is a good diagnostic to distinguish horizontal reflectors in the subsurface from diffraction hyperbolas, multiple reflections, and dipping interfaces. Only the primary reflections from subhorizontal interfaces will align horizontally after the NMO correction. Diffracted arrivals from a lateral discontinuity are illustrated in Figure 6.14. Notice they do not exhibit the normal moveout behavior.

The traveltime equations must be modified if a dipping reflector is present. Consider the path of the primary reflected ray associated with a dipping interface, as shown in Figure 6.15. The location of the reflection point P on the interface is determined by the requirement that the angle of ray incidence, measured with respect to the normal to the interface, equals the angle of reflection. Notice that the geophone (RX) in Figure 6.15 is placed down-dip from the seismic source (TX). Alternatively, a geophone could be placed up-dip from the source.

The down-dip traveltime τ_D from TX to RX is readily computed as the length of the seismic ray path divided by the velocity V of the medium which it traverses. To facilitate the computation and to gain further insight into seismic imaging of a dipping interface, it is

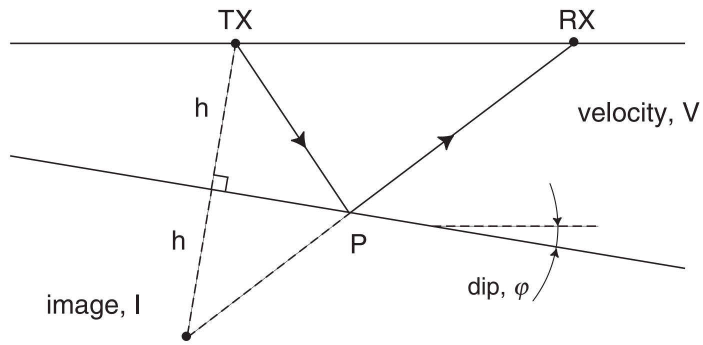

Figure 6.15 Primary reflection from a dipping interface.

useful to introduce the hypothetical image source I shown in the figure. The image source I is placed at the same perpendicular distance h from the dipping interface as the actual source TX. The traveltime τ_D is then calculated using the distance from the image I to the geophone RX as if the image were embedded in a homogeneous medium of velocity V. The result, using the law of cosines, is

$$\begin{aligned}\tau_D = \frac{\text{dist}\,(I - RX)}{V} &= \frac{1}{V}\sqrt{x^2 + (2h)^2 - 2x\,(2h)\,\cos\left(\frac{\pi}{2} + \varphi\right)} \\ &= \frac{2h}{V}\sqrt{1 + \left(\frac{x^2 + 4hx\,\sin\,\varphi}{4h^2}\right)};\end{aligned} \tag{6.26}$$

where x is the distance from TX to RX and φ is the dip angle. Notice that the angle at TX subtended by I and RX is $\pi/2 + \varphi$ [rad]. Similarly, if the source location is kept the same but the geophone RX is now moved to the other side of the TX, such that the seismic ray path is up-dip, the traveltime becomes

$$\tau_U = \frac{2h}{V}\sqrt{1 + \left(\frac{x^2 - 4hx\,\sin\,\varphi}{4h^2}\right)}. \tag{6.27}$$

The dip angle φ can be estimated in practice by measuring both seismic traveltimes τ_U and τ_D; this is accomplished by first placing the TX up-dip from the RX array, and then locating the TX down-dip.

6.9 Vertical and horizontal resolution

According to the Rayleigh criterion (Zeng, 2009), the *vertical resolution* of seismic waves is $\sim\lambda/4$, where $\lambda = V/f$ is the seismic wavelength. The frequency f is the dominant, or central, frequency carried by the seismic wave packet. For a typical near-surface geophysical application, with seismic waves propagating in a material of velocity $V = 1.5$ km/s at $f = 300$ Hz,

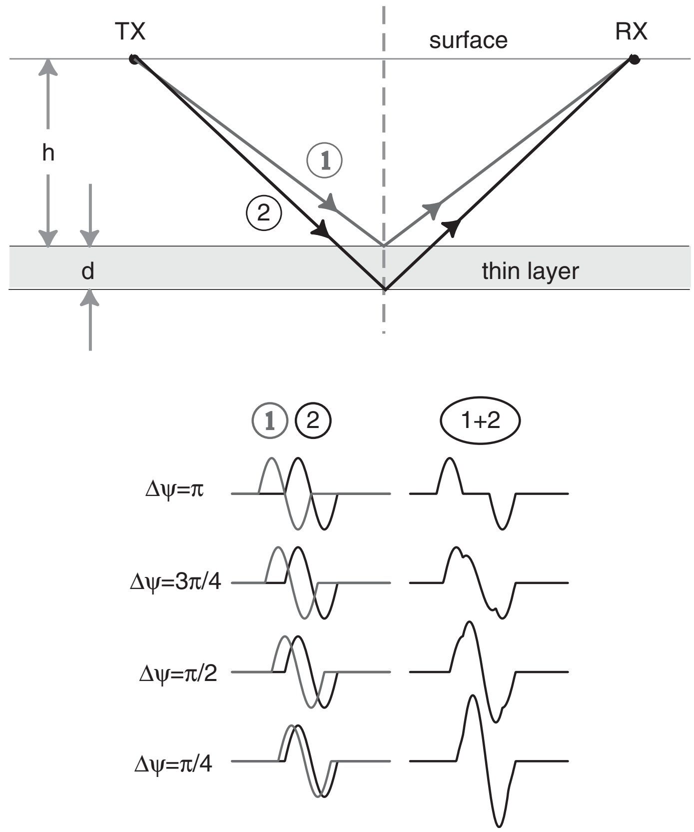

Figure 6.16 Resolution of a thin layer.

the seismic wavelength is 5.0 m. Hence, the vertical resolution is approximately 1.25 m. This means that two interfaces separated by less than 125 cm cannot be individually resolved by the returned seismic signal, as measured by a geophone. This result can be contrasted with exploration-scale geophysics in which dominant source frequencies are commonly 30 Hz or lower. In that case, the seismic wavelength in the same material is greater than 50 m, such that interfaces separated by less than 12.5 m cannot be individually resolved.

While the thickness of a fracture in a rock may not be resolved if the aperture is less than ~ 125 cm, the fracture certainly could be detected as an acoustic impedance discontinuity if the seismic properties of the fracture fill materials contrast sufficiently to those of the host material. In this sense, the ability to detect a fracture must be distinguished from the ability to determine its aperture.

The vertical resolution of a thin layer is illustrated in Figure 6.16 using an idealized seismic wave packet consisting of a single sinusoidal pulse. Of course, no practical seismic source could generate such an idealized packet; it is employed here simply to illustrate the concept of vertical resolution. The primary ray path 1 in Figure 6.16 indicates a reflection from the top of a thin layer of thickness d whereas the primary ray path 2 shows a reflection from the bottom of the thin layer. The slight difference in the lengths of paths 1 and 2 is manifest as a difference in phase ψ of the two seismic wave packets recorded by the geophone RX. The greater the difference in path length, the greater the difference in phase. If the phase difference is $\Delta\psi < \pi$, the two arrivals are somewhat merged together in the resulting geophone response (which is the sum of the two waves 1 and 2; shown as "1 + 2" in the bottom part of the figure). The geophone response resolves the thin layer as two separate arrivals only as the phase difference increases beyond $\Delta\psi > \pi$. The critical phase difference $\Delta\psi = \pi$ corresponds to a path-length difference of one-half the seismic wavelength, $\lambda/2$. A full wavelength λ would change the phase of the seismic wave packet by 2π. Thus, keeping in mind that the geophone response records the two-way traveltime of seismic wave arrivals, the layer thickness must satisfy $d > \lambda/4$ in order for it to be seen as two distinct events on a geophone. This result is strictly valid for small TX–RX offsets x such that $x << h$, where h is the depth to the top of the thin layer.

The *horizontal resolution* of the seismic-reflection method intuitively cannot be better than $\sim \Delta x/2$, where Δx is the geophone spacing. However, a straightforward analysis indicates that the horizontal resolution of an interface at depth h beneath the surface can also not be better than the Fresnel-zone radius

$$D_0 \sim \sqrt{2\lambda h}, \tag{6.28}$$

which is often larger than $\Delta x/2$. A simple justification of Equation (6.28) can be made as follows. Seismic energy emanates from a source TX into the subsurface in all directions. Three particular ray paths are shown in Figure 6.17a. The path labeled 1 is the primary reflection, and is the fastest purely reflected path to the geophone. A certain amount of energy, however, is carried in the two paths labeled 2 since, in reality, the reflection is not from an idealized point (Lindsey, 1989) but is generated by integration over a circular area which might be termed the seismic footprint. This accords with an extended Huygens principle (Sein, 1982) in which the incident planar wavefront, where it strikes the interface at a given location, acts as a source of downward-propagating refracted spherical wavelets and upward-propagating reflected spherical wavelets.

As shown in the figure, the two rays labeled 2 strike the reflecting interface at a distance $\pm D/2$ from the primary reflection point at the TX – RX midpoint. Energy carried along these two paths arrives somewhat later than energy carried along path 1. If the phase difference between either of the wave packets propagating along ray path 2 and the wave packet propagating along ray path 1 satisfies $\Delta\psi < \pi$, then the geophone response will not see these packets as distinct arrivals but rather they will appear merged together.

The horizontal resolution at a given depth h is therefore defined as the horizontal distance D along a reflecting horizon within which all reflected energy recorded at a given geophone arrives with phases that are within π of each other. The horizontal resolution is usually referenced to the zero-offset configuration in which the TX–RX separation distance is $x = 0$, but it can also be defined for a given non-zero offset x, as we show in the following.

The length of ray path 1 in Figure 6.17a is given by

$$l_1(x) = 2\sqrt{h^2 + \left(\frac{x}{2}\right)^2} \tag{6.29}$$

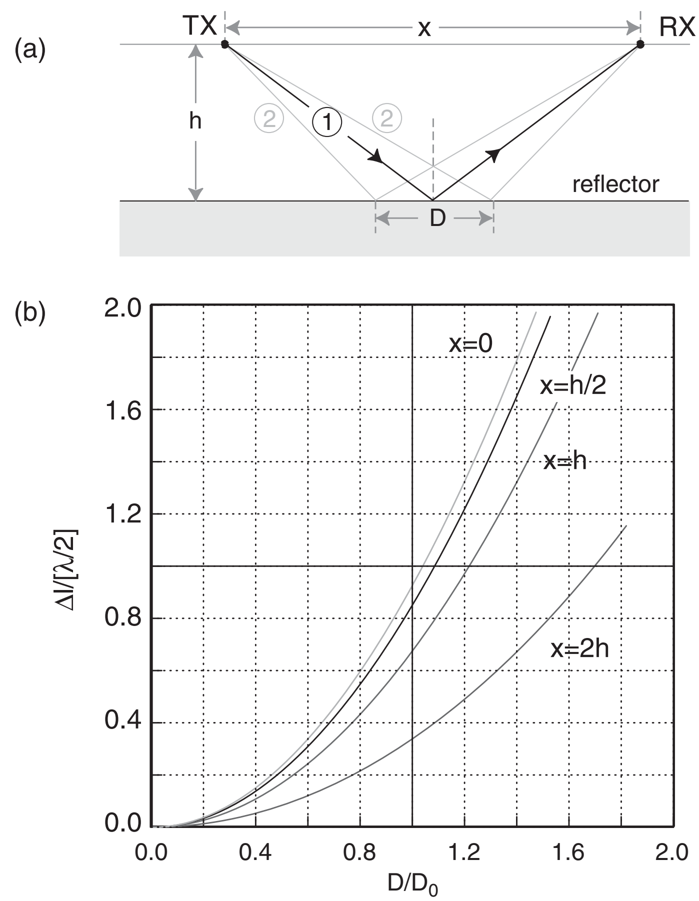

Figure 6.17 Horizontal resolution of the seismic-reflection method. (a) Fresnel-zone concept; (b) Path length difference Δl as a function of horizontal distance D.

while the length of either of the ray paths labeled 2 is given by

$$l_2(x) = \sqrt{h^2 + \frac{(x-D)^2}{4}} + \sqrt{h^2 + \frac{(x+D)^2}{4}}\,. \tag{6.30}$$

The difference $\Delta l = l_2 - l_1$ in the two path lengths, normalized by one-half the seismic wavelength $\lambda/2$, is plotted in Figure 6.17b versus the horizontal distance D/D_0 along the reflecting horizon. The parameters $h = 10$ m and $\lambda = 1.6$ m were chosen such that $D_0 \sim \sqrt{32} \sim 5.5$ m, using Equation (6.28). Different curves are plotted for different TX–RX separation distances x.

Notice that the curve for the zero-offset configuration $x = 0$ passes very close to the critical point $\Delta l = \lambda/2$ when $D = D_0$. This indicates that the horizontal resolution is given, to a very good approximation, by Equation (6.28) in this case. The graph in Figure 6.17b also shows that the horizontal resolution worsens as the TX–RX separation distance x increases. For example, consider the curve for the case $x = 2h$. The curve crosses the critical point $\Delta l = \lambda/2$ at $D \sim 1.7D_0 \sim 9.35$ m. This indicates that the horizontal resolution is

70% worse in the case $x \sim 2h$ compared to the ideal zero-offset case. In other words, the lateral resolution of the seismic-reflection method degrades with increasing distance between the shotpoint and the receiver. It makes intuitive sense that the seismic footprint should grow larger as the incident angle becomes shallower.

6.10 Common midpoint profiling

The accuracy of a reflector image can be improved if the seismic shotpoints and receivers are arranged such that each location along the reflecting horizon is illuminated from a number of different perspectives. This is readily accomplished using the common midpoint (CMP) profiling method. CMP data acquisition involves moving the shotpoint and receiver array forward in regular increments and shooting at each successive move. A subset of the resulting shot records can then be selected to simulate an acquisition that consists of a symmetric configuration of n seismic TX–RX pairs about a common midpoint P, as shown in Figure 6.18. In other words, individual traces that share a common midpoint are collected from the various shot records. This is termed a *CMP gather*. The benefit of this procedure is that a single reflection point on a subsurface interface is sampled n times. A CMP profile constructed in this manner is said to have n-fold data coverage.

After NMO corrections of the form (6.25) are applied, according to the TX–RX offset, each seismic trace in the CMP gather becomes effectively a zero-offset trace. The n NMO-corrected traces are then ready to be averaged, or *stacked*, to enhance the signal-to-noise (S/N) ratio. Generally, the improvement in S/N ratio due to stacking a number of traces acquired with the same TX–RX acquisition geometry can be understood as follows. Suppose the amplitude of a seismic-reflection signal is S, while the average noise amplitude is N. Assuming the noise to be random, the S/N ratio of the stacked trace is related to the S/N ratio of an individual trace by the fundamental formula

$$\frac{S}{N}(n) = \sqrt{n}\frac{S}{N}(1). \tag{6.31}$$

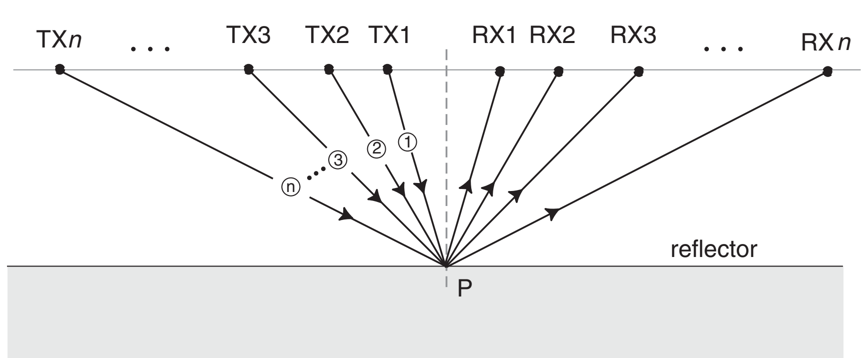

Figure 6.18 Common midpoint profiling, CMP.

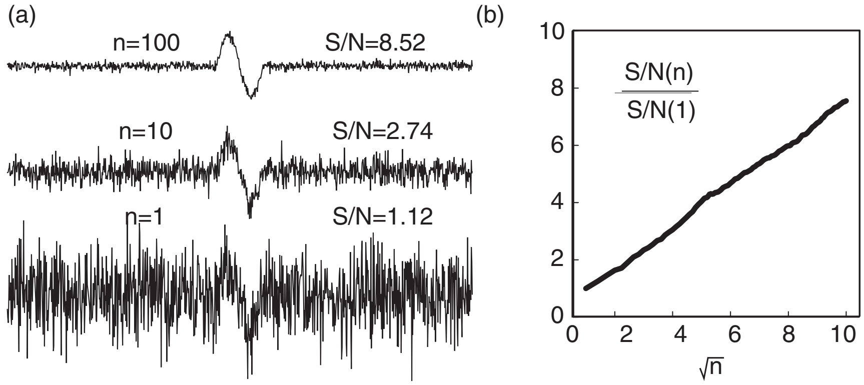

Figure 6.19 (a) Improvement of S/N ratio with stacking number n; (b) Plot of S/N-ratio improvement with $\sqrt{n}$.

There is a diminishing reward for increasing the stack number n, as shown by Equation (6.31). For example, doubling the S/N ratio requires stacking four shot records. Increasing the S/N by an order of magnitude requires stacking 100 shot records.

The effect of stacking on an idealized seismic trace that consists of a single sinusoidal pulse signal embedded in random noise is shown in Figure 6.19a. The signal occupies the middle 10% of the trace, as can be seen in the figure. The background noise is generated by a Gaussian random-number generator. The S/N ratio is *defined* in this case to be the rms (root mean squared) amplitude of the middle 10% of the trace divided by the rms amplitude of the remainder of the trace. It is evident from the figure that the S/N ratio increases with increasing stack number n, as expected. The sinusoidal pulse is easy to discern in the case $n = 100$, but difficult to detect visually in the case $n = 1$. The behavior of the S/N improvement, defined as the S/N ratio for n traces, normalized by the S/N ratio for a single trace, is shown in Figure 6.19b. Note that the "root-n" improvement in S/N ratio, as prescribed by Equation (6.31), is approximately satisfied.

CMP profiles with n-fold data coverage can offer a tremendous improvement in resolving subsurface reflectors relative to data of single-fold coverage. However, traditional CMP profiling quickly becomes laborious since it is necessary to uproot the entire array of n geophones and shift it forward by one station increment in order to advance the common midpoint by one station increment. CMP data acquisition is greatly simplified however with the use of a *roll-along switchbox*.

The effect of the switchbox is to automatically shift a geophone array by one station increment along a survey profile. Instead of manually picking up and moving the geophone array, the equivalent task can be accomplished simply by advancing the knob on the switchbox by one unit. The concept is illustrated in Figure 6.20. To keep the illustration simple, imagine an array of eight geophones connected via the switchbox to a four-channel seismograph (in practice, these numbers are more likely to be in the range of hundreds of geophones and tens or hundreds of channels). Suppose the four active geophones are RX1–RX4 when the switchbox is at position 1, as shown in the top part of the figure. Then, after the shot is recorded at this setting, the switchbox is advanced to position 2, thereby activating RX2–RX5. At the same time, the shotpoint (TX) is moved forward one station increment. This process continues until all switchbox settings have been used. The result

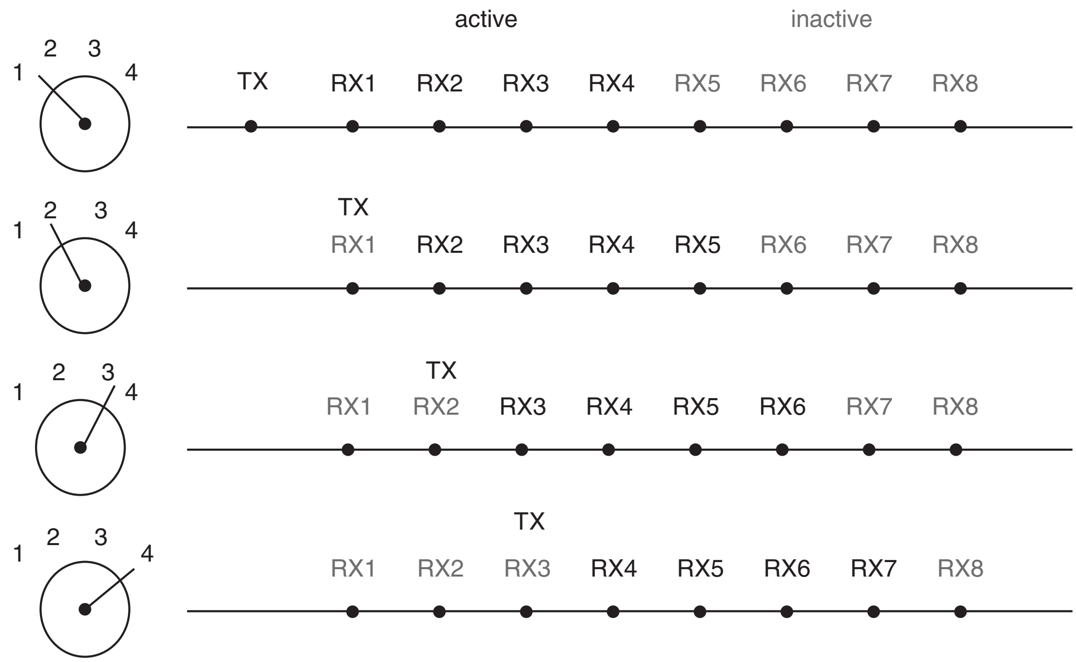

Figure 6.20 Roll-along data acquisition.

(a four-fold CMP profile) is the same as if a smaller array of four geophones had been manually shifted after each shot by one station increment.

6.11 Dip moveout

A major complication to CMP analysis occurs in the presence of *dipping reflectors*. In the presence of dip, the subsurface reflection point unfortunately is not the same for all common-midpoint TX–RX pairs (Figure 6.21). Notice that reflection points P_1 and P_2 are not coincident, and neither of the reflection points lie directly beneath the common midpoint. The NMO correction could be modified to accommodate a single dipping interface but more problematic is the case of multiple dipping reflectors that have different dip angles. Such cases are often encountered in aeolian or fluvial cross-bedded sedimentary systems or salt domes, for example, where gently dipping beds make contact with a steeply dipping structure. The CMP stacking process breaks down and the data quality actually deteriorates with increasing n. The imaging of multiple dipping reflectors can be greatly improved, however, by an application of *dip-moveout* (DMO) processing prior to performing the CMP stack. Here we outline just the essential concepts of DMO since the details of the algorithm are beyond the scope of the book. Good introductions to DMO are provided in Deregowski (1986) and Liner (1999).

The aim of NMO/CMP-stack processing is to identify, adjust the timing, and then gather traces that have the same reflection point on a subsurface reflector. If a dipping reflector of unknown dip angle is present, the location of the reflection point is not known, and hence a

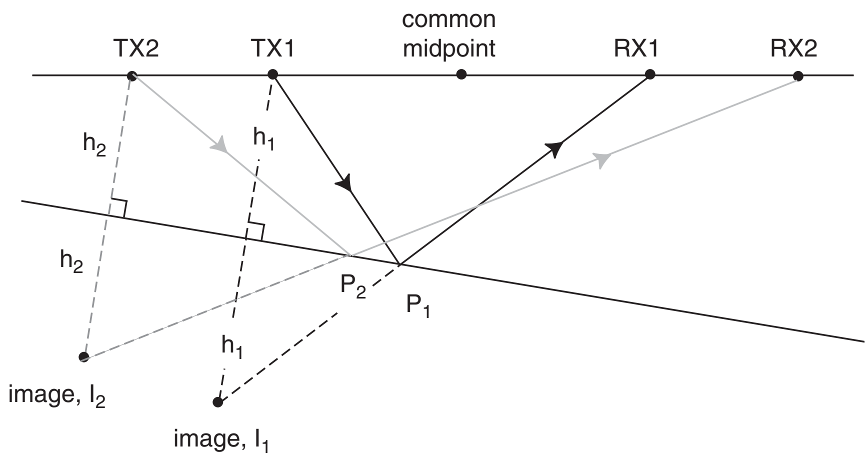

Figure 6.21 On a dipping reflector there is not a single point of reflection for all common-midpoint trace pairs, such as TX1–RX1 and TX2–RX2.

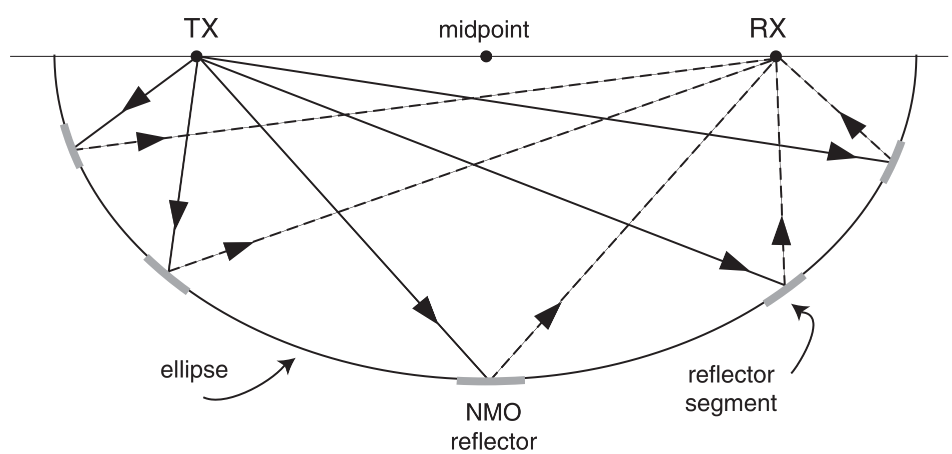

Figure 6.22 A reflection event seen at the RX can come from any point on the ellipse.

CMP gather cannot be made. However, only certain locations for the reflection point are possible. Simple geometry shows that the reflection point must be located on the ellipse in Figure 6.22, where the TX and RX are at each focus. A standard NMO correction assumes that the reflection originated from the horizontal segment located immediately below the midpoint. But each of the reflector segments shown in Figure 6.22 is an equivalent possibility, in the sense that they could equally explain the observed traveltime between the TX and RX.

The equivalent reflector segments are shown again in Figure 6.23a. The zero-offset locations (labeled 1–5) associated with each segment are also shown. In Figure 6.23b are shown the traces that would have been recorded had the TX and RX been co-located at each of the locations 1–5. These are the zero-offset traces, and the traveltimes of the first

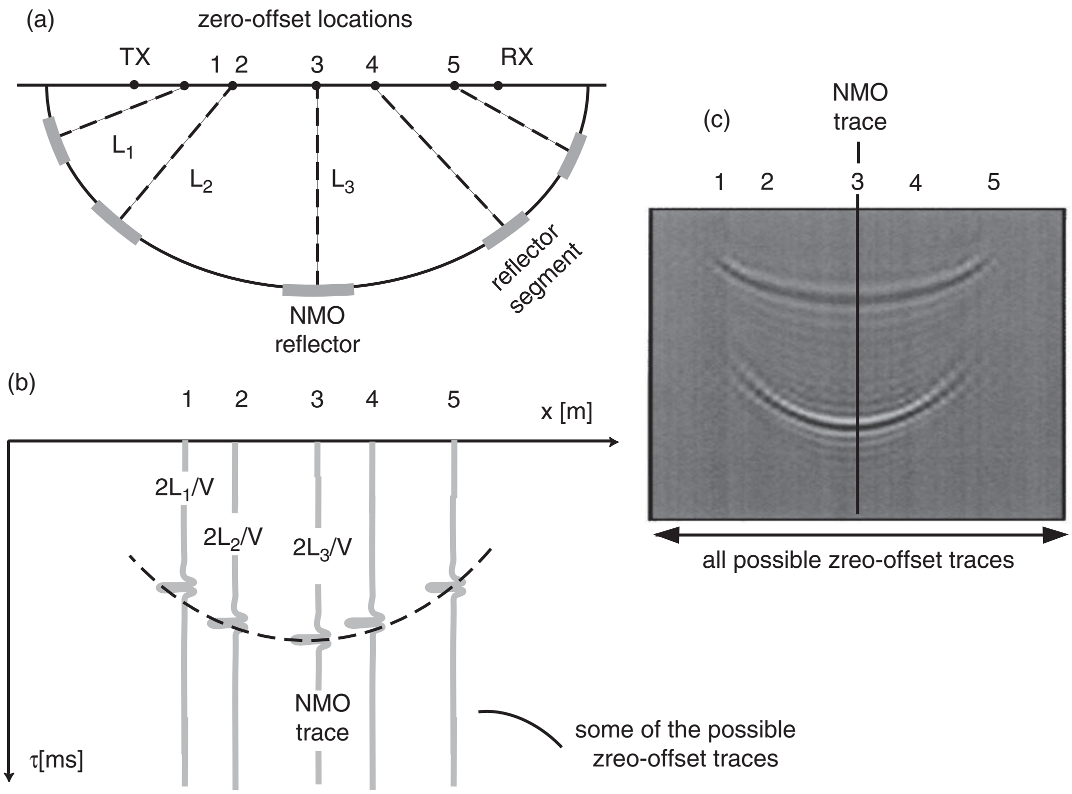

Figure 6.23 (a) Some of the possible zero-offset locations between the original TX and RX in the presence of a dipping reflector; (b) some of the zero-offset traces; (c) all possible zero-offset traces, for two dipping reflectors, forming two DMO smiles. After Liner (1999).

three of them are also indicated. The familiar NMO traveltime, for example, is $\tau_3 = 2L_3/V$. Since we don't know the actual dip of the reflector, we still don't know which one of these zero-offset traces to choose as the DMO-adjusted trace, but we do know that one of them must be correct.

Furthermore, the five zero-offset locations and traces that have been so far been considered are not the only possibilities. There are many other locations between the original TX and RX. In Figure 6.23c are shown all the possible zero-offset traces (actually, for two dipping reflectors). The portion of this plot that contains the highest amplitudes is whimsically known as a *DMO smile*, for an obvious reason. Again, this plot shows the zero-offset traces for every conceivable dip angle of the reflector.

The foregoing analysis shows that a single reflection event recorded on a single trace can be expanded into a multiplicity of zero-offset traces and then plotted to reveal a DMO smile. The NMO-corrected trace runs through the center of the DMO smile, as shown. By performing a similar DMO analysis on the next trace from the next TX–RX pair along the seismic survey profile, we can construct another DMO smile that partially overlaps the first one. In fact, we can construct an entire sequence of partially overlapping DMO smiles, one for every TX–RX pair along the seismic survey profile. Once we have all these DMO smiles, we simply add them together. This process produces the correct zero-offset image of the dipping reflector horizon in the subsurface. The stacking process works because the reflected energy from the actual dipping horizon is common to all of the DMO smiles such that constructive interference occurs when they are added together. Destructive interference occurs elsewhere. Hence, the correct trace from each of the DMO smiles is naturally selected by the stacking process. Interestingly, multiple dipping horizons with different dip angles are all correctly imaged and appear at their proper locations and orientations within the subsurface. Additional details, including a discussion of the close relationship between DMO and migration, is found in the tutorial article by Liner (1999), to which the interested reader is referred.

6.12 Attenuation

The theory of elasticity governed by Hooke's law predicts reversible stresses and strains in which no energy is lost during the transmission of a seismic wave. An ideal elastic wave nevertheless diminishes in amplitude as it propagates due to its *geometric spreading*. Moreover, its energy is *partitioned* as it is scattered by heterogeneities, and undergoes reflection, refraction, and P-to-S-wave conversion at acoustic impedance boundaries. Real seismic waves, however, continuously lose energy via the *absorption* of energy by the medium.

Consider a seismic wave propagating in a homogeneous medium and suppose that it has an amplitude A_0 at some distance r_0 from its source. Neglecting the scattering contributions, the amplitude of the wave at some greater distance $r > r_0$ from the source is given by

$$A(r) = A_0\left(\frac{r_0}{r}\right)\exp[-\alpha(r - r_0)], \qquad (6.32)$$

where the geometric spreading is described by the $1/r$ falloff and the exponential decay is due to energy absorption with attenuation coefficient α.

The $1/r$ form of the geometric spreading term in Equation (6.32) is due to the fact that the seismic energy associated with a spherical wave at some distance r from a source is distributed over the surface of a sphere of radius r. The surface area of a sphere is $4\pi r^2$. Hence, the seismic energy should fall off as $1/r^2$. The seismic energy is proportional to the square of the wave amplitude, hence the latter decreases as $1/r$. This energy-loss mechanism is termed geometric spreading since it is independent of the elastic properties of the medium.

The seismic attenuation coefficient α, on the other hand, does depend on the elastic properties of the medium and also on frequency. The physical causes of intrinsic seismic attenuation are not fully understood. Friction has been suggested as an absorption mechanism. Recent developments in the theory of *poroelasticity* propose that a large portion of the intrinsic loss in a saturated porous medium is caused by viscous fluid motions that arises in response to mechanical wave excitation (e.g. Pride *et al*., 2004). This mechanism is termed wave-induced fluid flow. In the scenario described by Muller

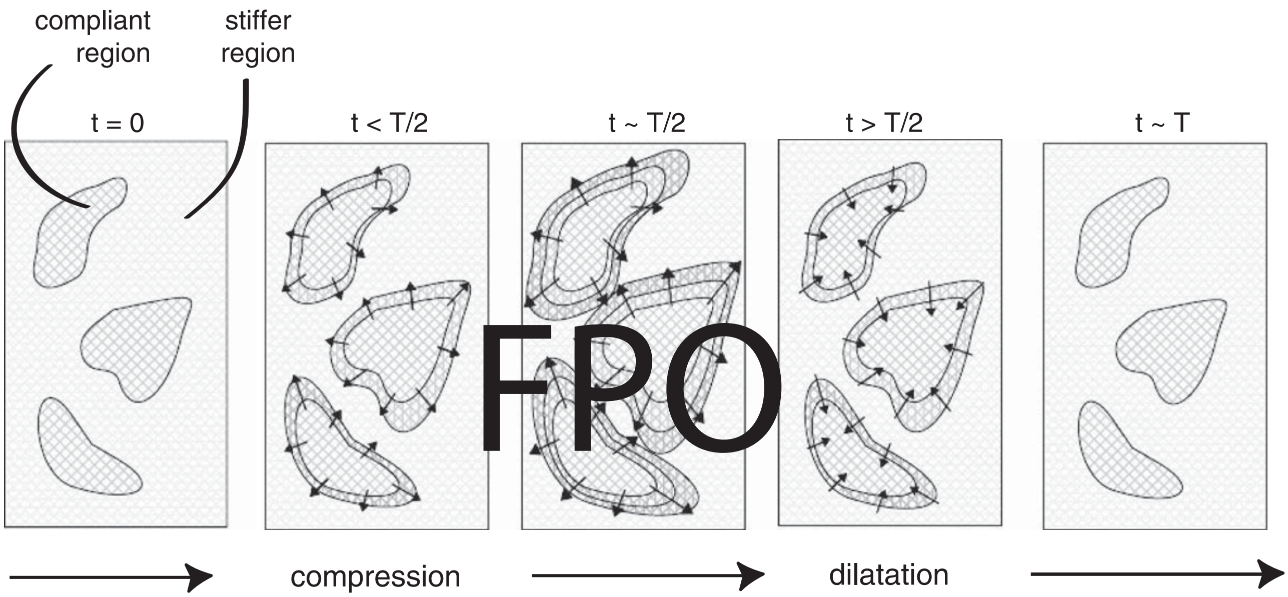

Figure 6.24 Seismic attenuation caused by wave-induced fluid flow in association with mesoscopic heterogeneities, after Muller *et al*. (2010).

et al. (2010) and depicted in Figure 6.24, fluid flows from compliant regions toward stiffer regions (as shown by the arrows in the second and third panels) during the compressional portion of an elastic wave cycle of period *T*, and vice versa during the expansive, or dilatational portion of the cycle (shown in the fourth panel). Wave-induced fluid flow as an attenuation mechanism is thought to be particularly effective in geomaterials for which the length-scale of the heterogeneities is *mesoscopic*, that is, the heterogeneities are much larger than typical pore sizes but smaller than the seismic wavelength. Decisive field-scale studies which permit the elaboration of the physical mechanisms responsible for attenuation of seismic wavefields have not yet been carried out in near-surface geophysics.

The attenuation of higher-frequency waves is much larger than that of lower-frequency waves. Typical values of the attenuation coefficient vary from $\alpha \sim 0.25$–0.75 decibels/wavelength [dB/m]. Thus, at large ranges compared to the longest seismic wavelength excited by the source, seismic pulses tend to become smoothed out and are of apparently long duration. In this sense, the Earth acts as a *low-pass filter*.

In a *viscoelastic* medium subject to a shear stress, the material undergoes some permanent shear deformation. Other types of irreversible seismic responses are possible in the presence of large strains or strain rates, including brittle failure, buckling or bending of engineered structures, various types of plastic deformation, and soil or sand liquefaction. The inelastic deformation of near-surface geomaterials in response to conventional seismic imaging sources such as hammers, shotguns, and vibrators is normally insignificant and is neglected in most active-source near-surface geophysical surveys.

6.13 Seismic refraction

The seismic-refraction method is similar to the reflection technique, the primary difference being that arrival times of horizontally refracted waves instead of near-vertical reflected waves are analyzed. The TX–RX offsets in refraction studies are generally larger than those of reflection studies, with the result that the slow-moving surface waves, or *ground roll*, is much less of a concern. The seismic-refraction method is a simple and popular technique used by geophysicists, geotechnical engineers, and others to gather basic site geological information such as depth to bedrock beneath an unconsolidated overburden.

Consider again seismic excitation of the two-layer model shown in Figure 6.11; in particular, we are now interested in the ray path labeled 3. The ray incident at some critical angle i_C travels along the interface as a P-wave with velocity V_2. The angle of refraction is equal to $r_C = 90°$. This is shown as the horizontal portion of ray path 3 in Figure 6.11. From Snell's law, written in the form

$$\frac{\sin i_C}{V_1} = \frac{\sin r_C}{V_2}, \tag{6.33}$$

with $\sin r_C = 1$, the critical angle is given by

$$i_C = \sin^{-1}\frac{V_1}{V_2}. \tag{6.34}$$

As the critically refracted wave propagates along the subsurface interface, energy is transmitted continuously into the upper and lower layers in accordance with Huygen's principle. At some RX location on the surface, sufficiently far from the TX, the first arrival of seismic energy is that which has emerged from the interface at the same critical angle i_C. This is shown as the upward portion of ray path 3 in Figure 6.11.

For small TX–RX separations, the first arrival is the direct *P*-wave, shown as ray path 1 in Figure 6.11. However, at some critical separation distance, $x = x_C$, known as the *cross-over distance*, the direct wave is overtaken by the critically refracted wave. The latter is sometimes known as a *head wave* since it is the first to arrive at RX locations in the region $x > x_C$.

From an inspection of the geometry of ray path 3 in Figure 6.11, it is straightforward to show that the traveltime $T(x)$ of the head wave is

$$T(x) = \frac{2h}{V_1 \cos i_C} + \frac{x - 2h \tan i_C}{V_2}. \tag{6.35}$$

The first term in the above equation originates from the upward and downward portions of the ray path while the second term corresponds to the horizontally propagating part. Using Snell's law for critical refractions in which

$$\sin i_C = \frac{V_1}{V_2}; \tag{6.36a}$$

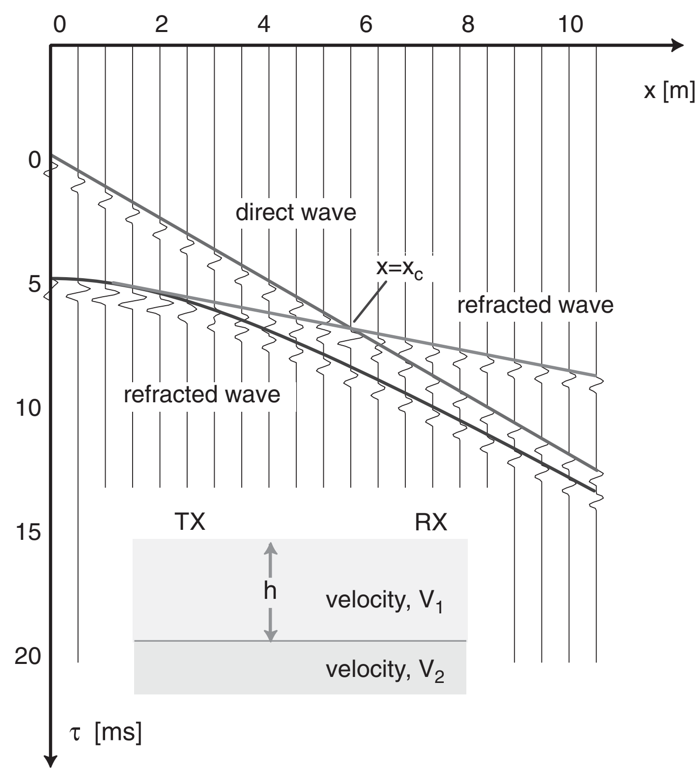

Figure 6.25 Idealized refraction seismogram.

$$\cos i_C = \frac{\sqrt{V_2^2 - V_1^2}}{V_2}; \tag{6.36b}$$

$$\tan i_C = \frac{V_1}{\sqrt{V_2^2 - V_1^2}}; \tag{6.36c}$$

Equation (6.35) reduces to

$$T(x) = \frac{x}{V_2} + \frac{2h\sqrt{V_2^2 - V_1^2}}{V_1 V_2}. \tag{6.37}$$

The traveltime Equation (6.37) predicts that refracted waves, unlike the hyperbolic moveout of reflected waves, move out linearly with TX–RX separation x. The slope of the $T(x)$ curve is $1/V_2$. Thus, one can obtain V_1 from the slope of the direct-wave arrival (which moves out according to $T(x) = x/V_1$) and V_2 from the slope of the head-wave arrivals. The layer thickness h can be determined by extrapolating the head-wave arrival back to the origin since

$$T_0 = T(0) = \frac{2h\sqrt{V_2^2 - V_1^2}}{V_1 V_2}. \tag{6.38}$$

The moveout curves of the direct wave, critically refracted wave, and reflected wave are illustrated in the idealized seismogram (shot gather) shown in Figure 6.25. The parameters

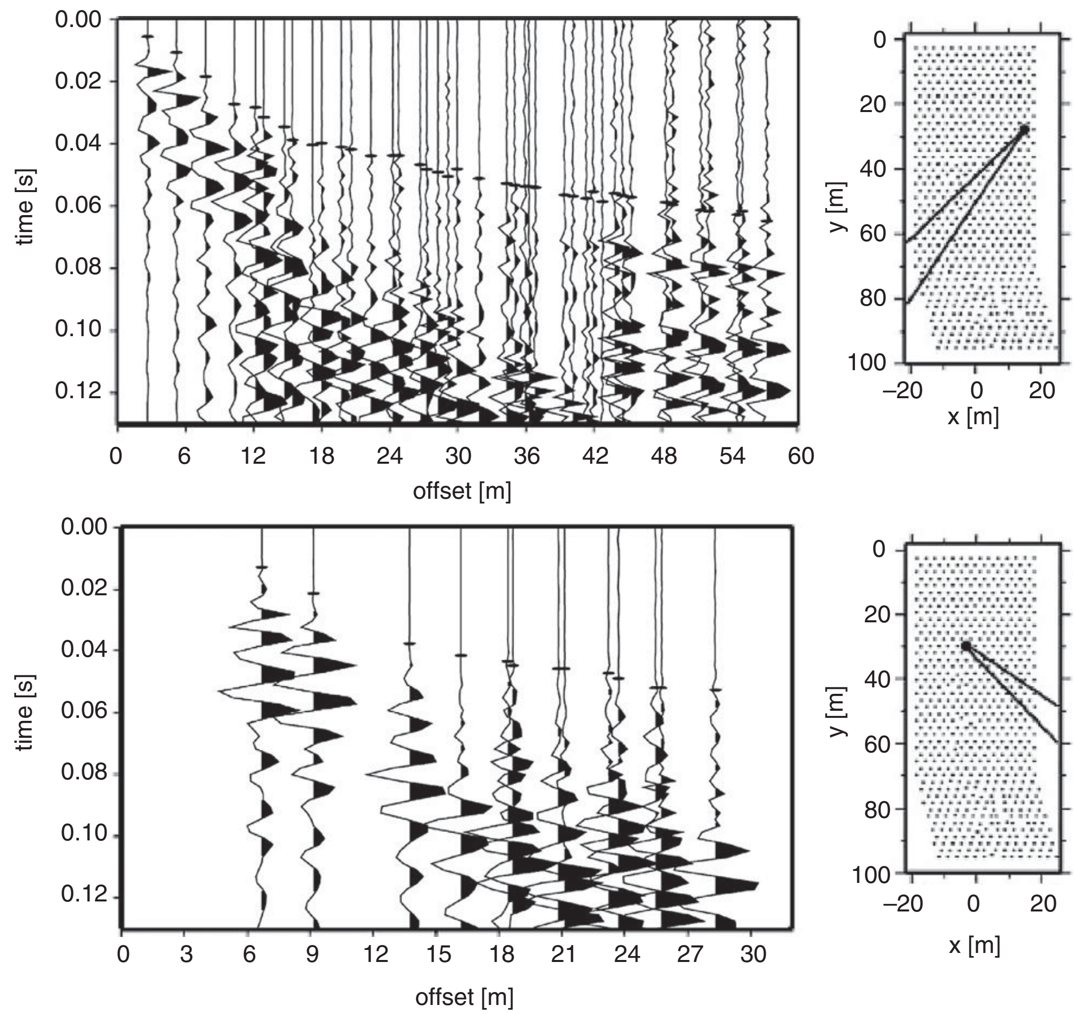

Figure 6.26 Shot gathers showing manually picked first arrivals (left panel), denoted by horizontal marks on the traces, from a seismic-refraction study at a contamination site; (right panel) shotpoints are marked by dark symbols; receivers are selected within a narrow TX–RX azimuth defined by the dark lines. After Zelt *et al*. (2006).

$V_1 = 800$ m/s; $V_2 = 2500$ m/s and $h = 2$ m were chosen for the calculation. Notice that the refracted wave is the first arrival beyond the cross-over distance x_C at which the direct and refracted arrivals are simultaneous. The primary reflected arrival is never the first arrival. Notice also that the refracted arrival does not appear on the traces at short TX–RX offsets, $x < 2h \tan i_C$. Instead, it merges with the primary reflection arrival, as shown in the figure. This behavior is easily understood by an inspection of ray path 3 in Figure 6.11.

In seismic-refraction studies, first arrivals are typically picked manually from observed shot gathers. This can become a time-consuming process for large two- and three-dimensional (2-D and 3-D) surveys. In addition, it is not always possible to precisely identify the first-arriving energy as, by definition, it is a small signal and moreover it often occurs in the presence of noise. Examples of first-arrival picks are provided in Figure 6.26 (left panels) from a 3-D refraction experiment at a contaminated site by Zelt *et al*. (2006). The picked first arrivals are shown by the horizontal markers on the individual traces of the shot gathers. Figure 6.26 (right panels) shows the location of the two shotpoints (large

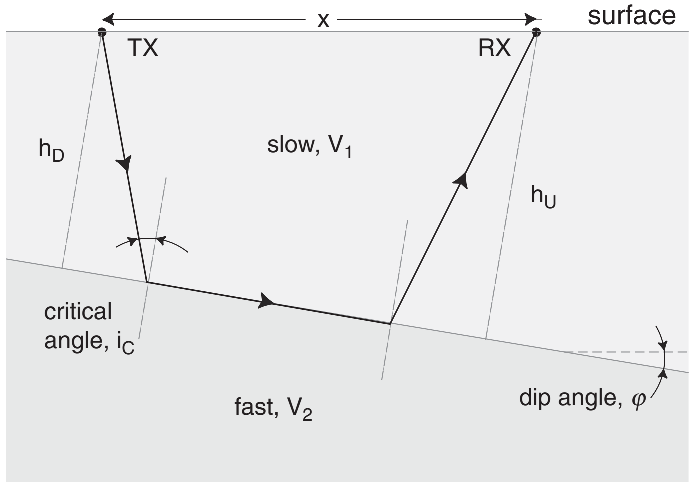

Figure 6.27 Seismic-refraction path for a dipping interface.

dots) relative to the locations of the receivers (small dots). The traces selected for display at the left are from those receivers located within narrow azimuthal cones of the shotpoints. The cones are marked by the solid lines in the right panels.

A dipping subsurface interface can also be analyzed using the seismic-refraction method. Consider the ray path shown in Figure 6.27. The RX is located down-dip from the TX. The dip angle φ measures the inclination of the subsurface bed. The lower medium has a faster seismic velocity than the upper medium. The dip angle φ can be estimated from measurements of up-dip and down-dip traveltimes. The head-wave traveltime curve $T_D(x)$ for a small dip angle φ such that $\cos^2\varphi \sim 1$ is given by

$$T_D(x) = \frac{2h_D \cos i_C}{V_1} + \frac{x \sin(i_C + \varphi)}{V_1}, \tag{6.39}$$

which shows that the down-dip refracted wave moves out with apparent velocity $V_D = V_1/\sin(i_C + \varphi)$. Similarly, the apparent up-dip velocity is $V_U = V_1/\sin(i_C - \varphi)$. The dip angle is then given by

$$\varphi = \frac{1}{2}\left[\sin^{-1}\left(\frac{V_1}{V_D}\right) - \sin^{-1}\left(\frac{V_1}{V_U}\right)\right]. \tag{6.40}$$

The derivation of Equation (6.40) is left as an exercise for the reader.

It is a simple matter to compute traveltime curves for a medium consisting of multiple refracting horizons. The two-layer case is illustrated in Figure 6.28 (bottom). Recall that the traveltime for a single refracted arrival, along the path labeled 1, can be written as

$$t_1(x) = \frac{x}{V_2} + \frac{2h \cos\theta_{C1}}{V_1}, \tag{6.41}$$

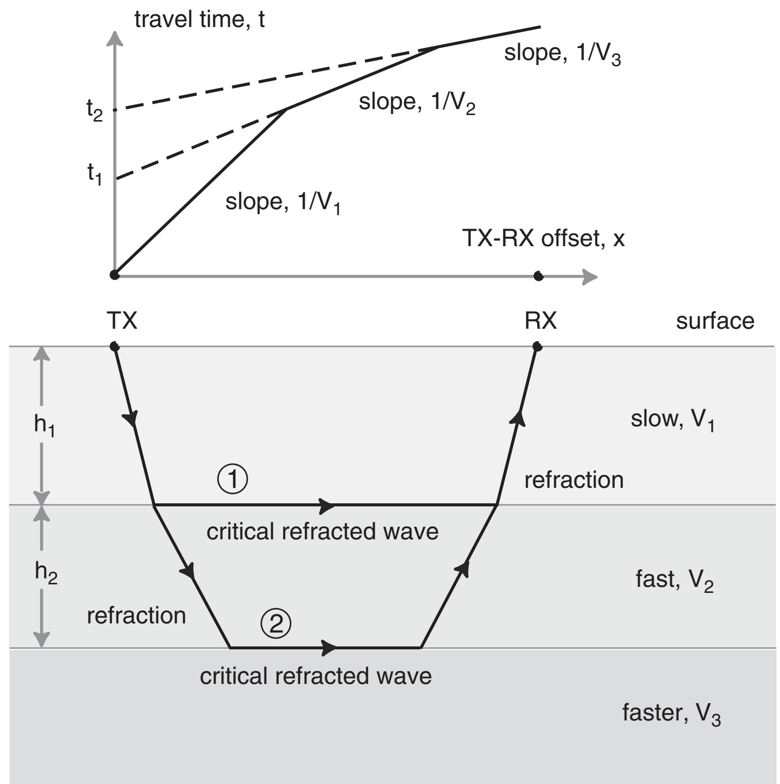

Figure 6.28 Traveltime curves (top) and ray paths (bottom) for the two-layer refraction geometry.

where θ_{C1} is the critical angle of refraction for the interface between media 1 and 2. The curve $t_1(x)$ of Equation (6.41) is shown as the middle straight-line segment in Figure 6.28 (top), with slope $1/V_2$.

Suppose that a layer of faster velocity $V_3 > V_2$ underlines the two-layer medium. At sufficiently large TX–RX offsets, the deeper refraction will eventually overtake the shallower refraction. The traveltime curve $t_2(x)$ for the refraction along the path labeled 2 is readily computed by applying Snell's law at each of the interfaces to determine the path geometry,

$$\frac{\sin\theta_{C1}}{V_1} = \frac{\sin\theta_{C2}}{V_2} = \frac{1}{V_3}. \tag{6.42}$$

where θ_{C2} is the critical angle of refraction for the interface between media 2 and 3. It is straightforward to generalize the traveltime curve to the case of an n-layer medium. The result is

$$t_n(x) = \frac{x}{V_n} + \sum_{i=1}^{n-1} \frac{2h_i \cos\theta_{Ci}}{V_i}. \tag{6.43}$$

Note that Equation (6.43) provides an accurate description of the observed traveltime curve only in the case in which each bed layer is fast enough and thick enough to contribute first-arriving energy over a significant portion of the overall time–distance curve to permit its slope to be analyzed correctly. It is possible to have a "hidden layer" in a standard refraction analysis. In such cases, the hidden bed is either too thin or its velocity is not sufficiently greater than those of the overlying beds to contribute a first arrival at any TX–RX offset distance x.

6.14 Practical considerations

The seismic-reflection and -refraction methods work well in fine-grained, saturated sediments where attenuation is low and excellent mechanical coupling to the ground can be achieved by the source and the geophones. The methods fare relatively poorly in loose, dry, coarse-grained, or disturbed sediments.

A sample seismic record acquired at the Texas A&M University main campus in College Station is shown in Figure 6.29. A sledgehammer source was used with geophone spacing of 3.0 m. The near-surface geology consists of ~ 10 m of heavy floodplain clay deposits overlying a soft plastic shale. This particular record shows a high-frequency (>100 Hz) air wave with linear moveout traveling at its characteristic value of ~ 330 m/s; a refracted head wave traveling at ~ 1735 m/s within the fast subsurface shale layer; possible reflected waves; and the ubiquitous low-frequency (20–30 Hz) dispersive ground roll traveling with velocities in the range ~ 160–313 m/s.

The choice of seismic source requires careful consideration. The frequency content of a seismic source depends on the near-surface geology and the source coupling to the ground. Good coupling may be attained with a sledgehammer source using a heavy strike plate with a large surface area. If explosives or a shotgun is used, the charge should be detonated in a tightly packed, water-saturated hole. The role of the water is to fill void spaces in which elastic energy would otherwise be dissipated. It is highly advised to test the performance of a number of different sources prior to conducting data acquisition over the full survey area. For imaging reflections from the uppermost 3–10 m of the subsurface, a source should produce significant energy at frequencies above ~ 250–300 Hz. Baker *et al*. (2000) compared the performance of various impulsive sources, including a 4.5 kg sledgehammer and two different rifles (30.06 and .22 caliber). At a test site in Kansas, the most coherent reflection images were obtained using the .22-caliber rifle with subsonic ammunition since this combination generated the largest amount of high-frequency energy. Important characteristics of some commonly used seismic sources are listed in Table 6.3.

An electromagnetic geophone (see Figure 2.3, left), which is the type of ground-movement sensor most commonly used in near-surface geophysics, detects the relative motion between a magnet and a coil. The magnet, being rigidly coupled to the plastic case of the geophone, is directly coupled to the ground. The coil is wrapped around the magnet and loosely coupled to it by means of a leaf spring. The movement of the magnet relative to that of the coil introduces, by Faraday's law of electromagnetic induction, an electromotive force (emf) in the coil which is recorded as an output voltage.

Good ground coupling of the geophone should be ensured using a long spike. The geophone should be firmly planted into solid or fully saturated ground beneath any organic litter or other poorly consolidated surface materials. Dry sand is a poor environment for geophones because of the high absorption of energy. A simple mechanical model of a geophone consisting of a series arrangement of parallel springs and dashpots is shown in Figure 6.30a. The theoretical response of the model mechanical system to a ground forcing of the form $F_0 \exp(i\omega t)$ is easily calculated (Krohn, 1984), as shown below.

Table 6.3 Seismic source characteristics			
Source	Repeatability	Frequency [Hz]	Cost
Hammer	Fair–good	50–200	$
Weight drop	Good	50–200	$$
Explosives	Fair	50–200	$$
Shotgun/rifle	Very good	100–300	$$
Vibrator	Poor	80–120	$$$

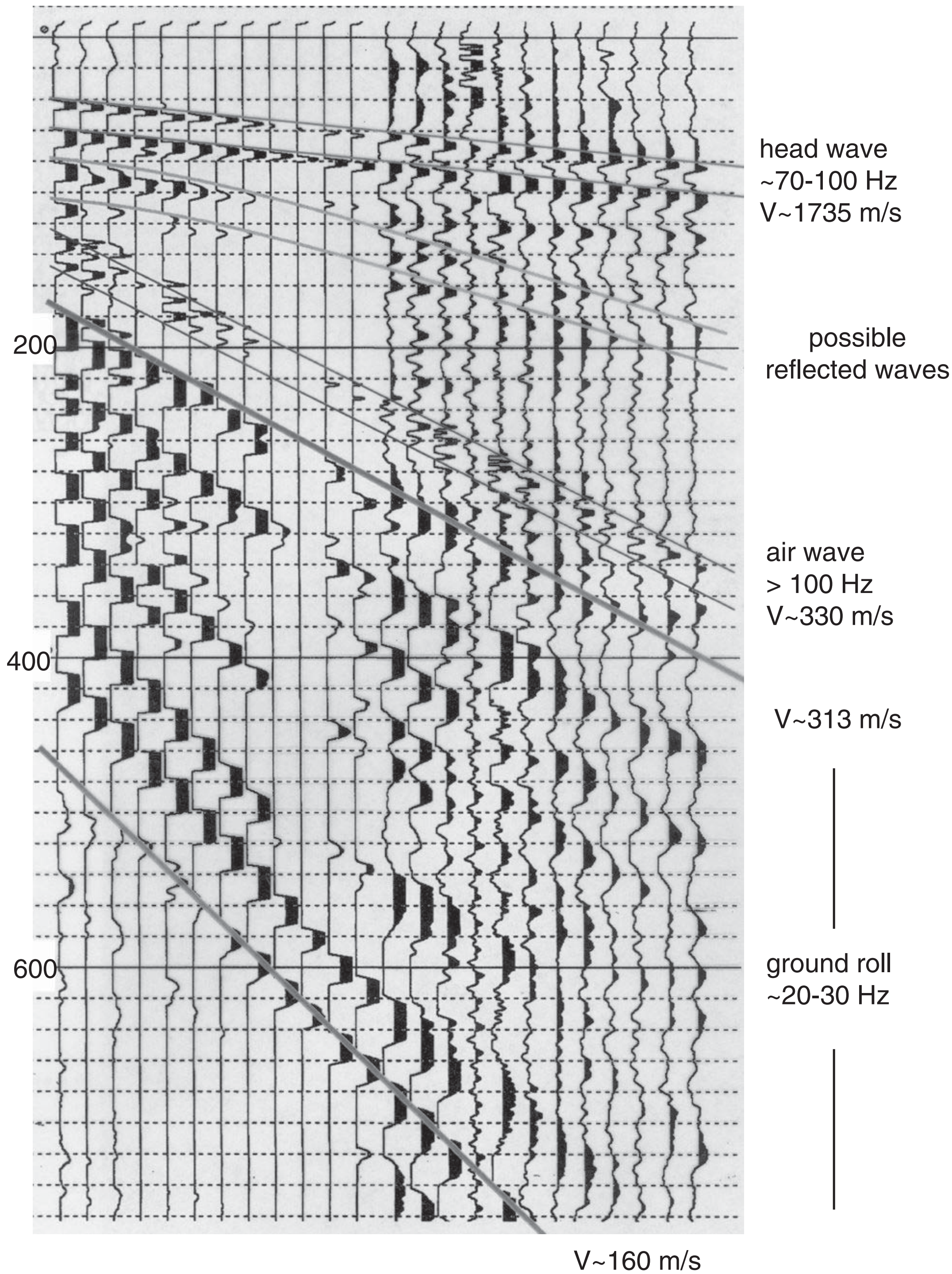

Figure 6.29 Seismic-reflection records at Texas A&M main campus. Adjacent traces are separated by 3.0 m. The vertical axis is two-way traveltime [ms].

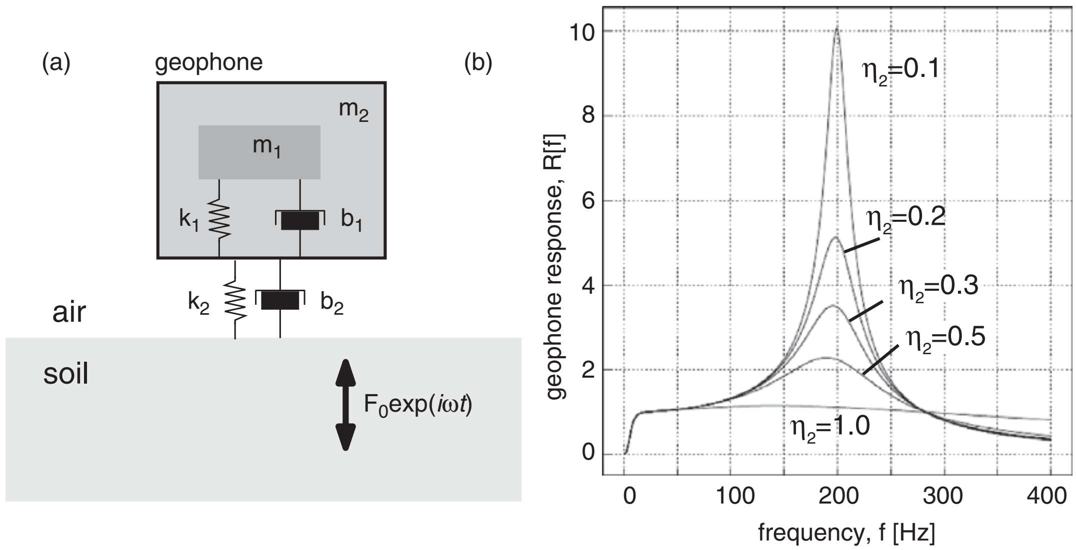

Figure 6.30 (a) A simple mechanical model of a geophone coupled to the ground; (b) calculated geophone response function amplitude $|R(f)|$ for different values of the ground damping factor, η_2.

Mechanical analysis of the geophone. As a first step, neglect the internal mechanisms inside the geophone and suppose the system to consist of a single undifferentiated mass m_2 undergoing damped oscillations in the presence of a driving force $F_0 \exp(i\omega t)$ that represents harmonic ground motion at frequency ω. The geophone is then approximated by a simple spring and a viscous resistance in parallel arrangement, see Figure 6.30a. The associated spring force is given by Hooke's law $F_S = -k_2\xi$ with spring constant given by k_2. The restoring force F_S is proportional to the displacement ξ of the geophone; as the spring is stretched, the force becomes stronger and acts in opposition to further extension.

Friction against the motion of the geophone due to its imperfect coupling to the ground results in damping of the oscillations. The friction force F_R is proportional to the velocity of the geophone (French, 1971) such that

$$F_R = -b_2 \frac{d\xi}{dt}, \tag{6.44}$$

where b_2 is the *mechanical resistance*. The negative sign indicates that the friction force opposes the motion of the geophone. The equation of motion for the damped oscillation is obtained by the force balance

$$m_2 \frac{\partial^2 \xi}{\partial t^2} + b_2 \frac{\partial \xi}{\partial t} + k_2 \xi = F_0 \exp(i\omega t), \tag{6.45}$$

which in the frequency domain has the solution

$$\xi(\omega) = \frac{F_0/m_2}{(\omega_2^2 - \omega^2) + i\omega\gamma_2}, \tag{6.46}$$

where $\gamma_2 = b_2/m_2$. In Equation (6.46), the parameter $\omega_2 = \sqrt{k_2/m_2}$ is termed the *resonant frequency*. The maximum amplitude of $\xi(\omega)$ will occur when the in-phase term in the denominator vanishes, that is, at the resonant frequency $\omega = \omega_2$. Note that the system is said to be *critically damped* if the special condition $\omega_2 = \gamma_2/2$ is met. The amplitude of the oscillations of a critically damped system is zero. Equation (6.46) is the complete solution for the displacement of a rigid mass m_2 undergoing damped oscillations driven by harmonic ground motion of the form $F_0 \exp(i\omega t)$.

Now the mechanical analysis should take into account the internal magnet and coil of the geophone. The internal spring constant is k_1 and the internal mechanical resistance is b_1. The magnet–coil system can be assumed to be driven by the motion of the external case, described by Equation (6.46), in which case a new balance of forces yields the equation of motion of mass m_1 in Figure 6.30a,

$$m_1 \frac{\partial^2 z}{\partial t^2} + b_1 \frac{\partial z}{\partial t} + k_1 z = m_2 \frac{\partial^2 \xi}{\partial t^2} = -b_2 \frac{\partial \xi}{\partial t} - k_2 \xi, \tag{6.47}$$

where z is the displacement of mass m_1. Since all terms in Equation (6.47) are harmonic with frequency ω, it is a simple exercise in algebra to solve this equation in the frequency domain. This results in the *geophone response function* $R(\omega)$ given by

$$R(\omega) = \frac{-\left(\frac{\omega}{\omega_1}\right)^2 \left[1 + i\left(\frac{\omega}{\omega_2}\right)\eta_2\right]}{\left[1 - \left(\frac{\omega}{\omega_1}\right)^2 + i\left(\frac{\omega}{\omega_1}\right)\eta_1\right]\left[1 - \left(\frac{\omega}{\omega_2}\right)^2 + i\left(\frac{\omega}{\omega_2}\right)\eta_2\right]}, \tag{6.48}$$

where $\eta_1 = \gamma_1/\omega$ is the *damping factor* of the magnet–coil system and $\eta_2 = \gamma_2/\omega$ is that of the ground coupling. The damping factor describes how close a system is to critical damping; the value $\eta = 0$ corresponds to free oscillations (no damping), while $\eta = 2$ corresponds to critical damping. Both the parameter $\gamma_1 = b_1/m_1$ and the resonant frequency $\omega_1 = \sqrt{k_1/m_1}$ of the geophone magnet–coil system are under control of the geophone designer. The physical significance of the response function $R(\omega)$ is that it is proportional to the acceleration of the mass m_1, that is, $R(\omega) \sim \omega^2 z(\omega)$.

The response function amplitude $|R(f)|$, where $f = \omega/2\pi$ is the frequency [Hz], is plotted in Figure 6.30b for different values of the ground-coupling damping factor η_2. A standard geophone is assumed in this calculation, with resonant frequency $\omega_1 = 8$ Hz and damping factor $\eta_1 = 1.4$, or 70% of the critical value. These are typical geophone design values. It is also assumed that the resonant frequency of the ground coupling is $\omega_2 = 200$ Hz. The figure illustrates the effect of imperfect ground coupling on the frequency response of a geophone. As the ground-coupling damping factor η_2 gets larger, the effect is an overall reduction in the amplitude of the geophone response and a flattening of the amplitude spectrum. A peak in the response function amplitude $|R(f)|$ indicates frequencies of ground motion to which the geophone is most sensitive. Thus, the effect of loose coupling of the geophone to the soil (i.e. a large value of η_2) is a great reduction in the sensitivity to the ground motion at its resonant frequency, in this case 200 Hz. The geophone therefore should be firmly planted in the soil, or buried, to keep the damping factor η_2 as low as possible.

Once the geophone output voltage is measured, the signal is amplified, filtered, and stored in a digitized form on a *seismograph*. The main characteristics of a seismograph are dynamic range and the number of channels. The dynamic range is the ratio of the largest measureable signal to the smallest measureable signal, as mentioned earlier in Chapter 2. Near-surface geophysical applications typically utilize 16-bit (20384, or 96 dB) dynamic range. The number of channels (usually 36–48, or more) is the number of geophones whose response can be simultaneously recorded.

6.15 Seismic data processing

A number of data processing steps must be performed in order to convert seismic-reflection shot gathers into migrated depth sections that are ready for geological interpretation. The discussion here will be brief. The classic reference for exploration-scale seismic data processing is Yilmaz (2001). The course notes of Baker (1999) provide a good overview of data-processing procedures that are relevant to near-surface geophysics. Chapters 2, 9, and 11 of this book also contain information on basic data processing.

Gain control. It is often required to amplify the small geophone signals recorded in a near-surface geophysical survey. Since seismic waves attenuate exponentially with distance, and are subject to spherical wavefront spreading, the return amplitudes from reflectors at depth are generally much lower than the amplitudes returned from shallower reflectors. Similarly, returns on the far-offset geophones are much smaller than those on geophones that are placed close to the source. Amplifier gains on each channel should be set in order to roughly equalize the signal amplitudes, thus permitting a better visualization of deeper reflectors especially at the far-offset geophones. This procedure is termed *gain control*.

Bandpass filtering. Filters may be used to suppress unwanted events and highlight events of interest on seismic-reflection records. The essentials of filtering were discussed earlier in Chapter 2. A number of filtering operations are specialized to seismic-reflection data processing. For example, *mutes* are routinely used to blank out refraction first-breaks, airwave and/or ground-roll energy from shot gathers. A *bandpass filter* reduces the amplitude of the frequency components of a signal that reside outside a specified band. In many cases, surface waves can be effectively removed by bandpass filtering. Surface waves are unwanted low-frequency events that can obscure or interfere with higher-frequency seismic reflections. An example of bandpass filtering of a shot gather acquired with a 1-kg hammer source at 0.25-m receiver spacing on the Matanuska glacier is Alaska is shown in Figure 6.31. The predominant frequencies are above 800 Hz for the wanted reflections from within the ice layer and from debris-rich ice at the base of the glacier, while the frequency content of the unwanted surface waves was considerably lower. Accordingly, a bandpass filter with pass band 700–1200 Hz proved effective in attenuating the surface waves while preserving the reflections, as shown on the right side of the figure. In this example, the surface waves were relatively non-dispersive with a group velocity of ~ 1700 m/s while the body waves traveled much faster, at 3600 m/s.

Refraction-statics correction. Refraction statics (Gardner, 1967) are adjustments that are made to the timing of individual seismic traces which take into account factors such as

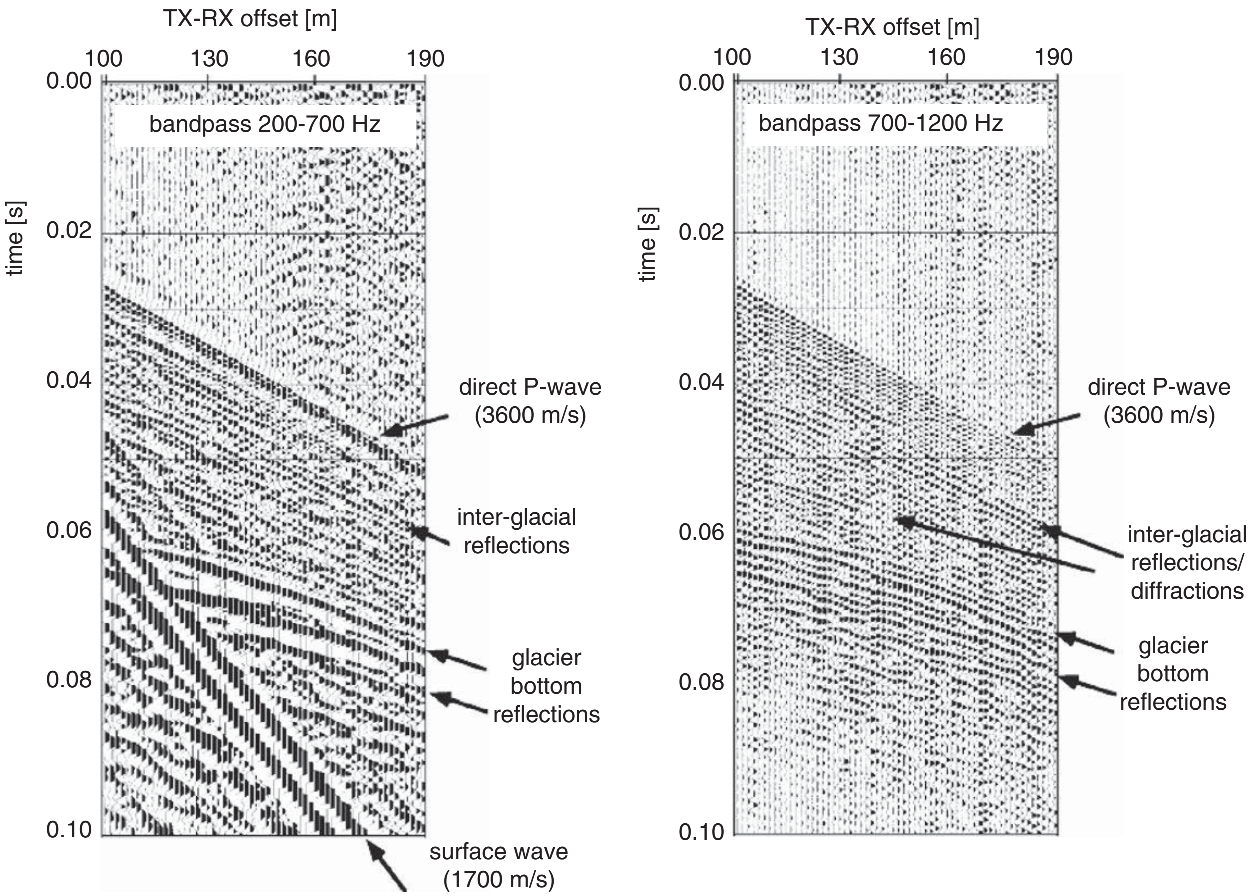

Figure 6.31 Surface-wave attenuation using bandpass filtering. After Baker *et al.* (2003).

near-surface lateral velocity variations, undulations of a shallow refracting horizon, and irregular terrain. The results of a refraction-statics correction are better estimates of the traveltimes to deeper reflectors. The new traveltimes are the ones that would have been recorded if the near-surface layer were homogeneous and/or the terrain and the shallow refracting horizon were level. With static-corrected data, deeper reflection events from horizontal layers generally exhibit an improved normal moveout, such that NMO stacks are more coherent than they would have been in the absence of the refraction-statics correction. Essentially, a refraction-statics correction enables better control on deeper reflector imaging by removing the deleterious effects of near-surface lateral velocity variations on traveltimes.

Docherty and Kappius (1993) have cast a refraction-statics correction into a linear inverse problem (see Chapter 11). In two dimensions, the situation they treat is illustrated in Figure 6.32. The observed refraction first-arrival traveltime t_{ij} between the TX–RX pair (i, j) is inverted for the down-going and up-going delay times (s_i and r_j, respectively) and the slownesses σ_k along the undulating refractor horizon. The latter is discretized into cells of width k. The delay time s_i is the time taken for the signal to propagate from the source down to the refractor horizon while the delay time r_j is the time taken for the signal to propagate upward from the refractor horizon to the receiver at the surface. The time-delay equations are

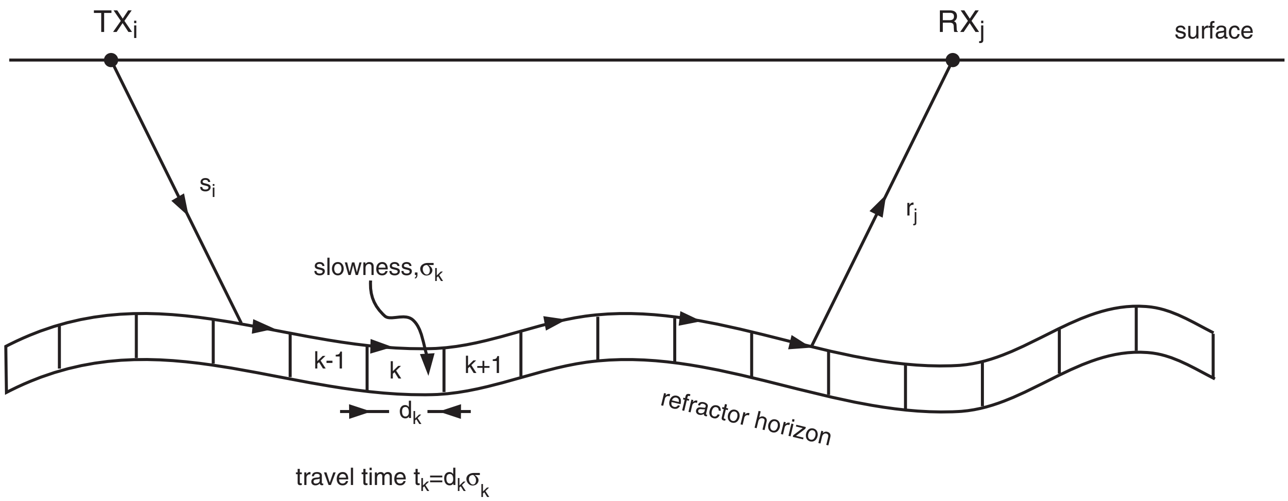

Figure 6.32 Refraction ray path associated with an undulating near-surface horizon for the (*i*, *j*)- th TX–RX pair.

$$t_{ij} = s_i + r_j + \sum_{k=1}^{P} d_k \sigma_k, \tag{6.49}$$

for each of the TX–RX pairs and P is the number of cells discretizing the refractor horizon. The equations in (6.49) constitute a set of linear constraints that connect the measured delay times t_{ij} to the unknown model parameters (s_i, r_j, σ_k). The system of equations can be solved using one of the linear-inversion techniques discussed later in Chapter 11.

Velocity analysis. Another critical step in the basic seismic data-processing sequence is to determine the *stacking velocity V* that should be used in the NMO correction (Equation (6.25)). Velocity analysis is a process that is performed on CMP gathers. Recall that a CMP gather is a collection of traces that contains reflections from the same point on a subsurface horizon; for horizontal strata, the reflection point lies directly beneath the common TX–RX midpoint. Velocity analysis can also be performed on *CMP supergathers*. A CMP supergather is a collection of adjacent CMP gathers plotted together. If lateral velocity variations are sufficiently small, all reflection points in a CMP supergather are presumed to reside within the same Fresnel zone on the subsurface horizon. Velocity analysis can also be performed in the presence of dipping layers, in which case the stacking velocity V is used in the DMO process.

In a simple form of velocity analysis known as *constant-velocity stacking* (CVS), the stacking velocity is presumed to be uniform throughout the subsurface. A sequence of regularly spaced values of stacking velocity is tried in the NMO correction procedure, with the optimal value being the one that best appears to flatten out the hyperbolas and provide good lateral continuity of reflectors on the CMP (super)gather. The CVS technique is normally applied manually, with the interpreter looking simultaneously and qualitatively comparing different CMP gather or supergather displays, each one having been NMO-corrected using a different stacking velocity.

A less subjective, automated method of velocity analysis involves the construction and analysis of a *semblance* plot. Semblance is a robust (noise-tolerant) measure of the

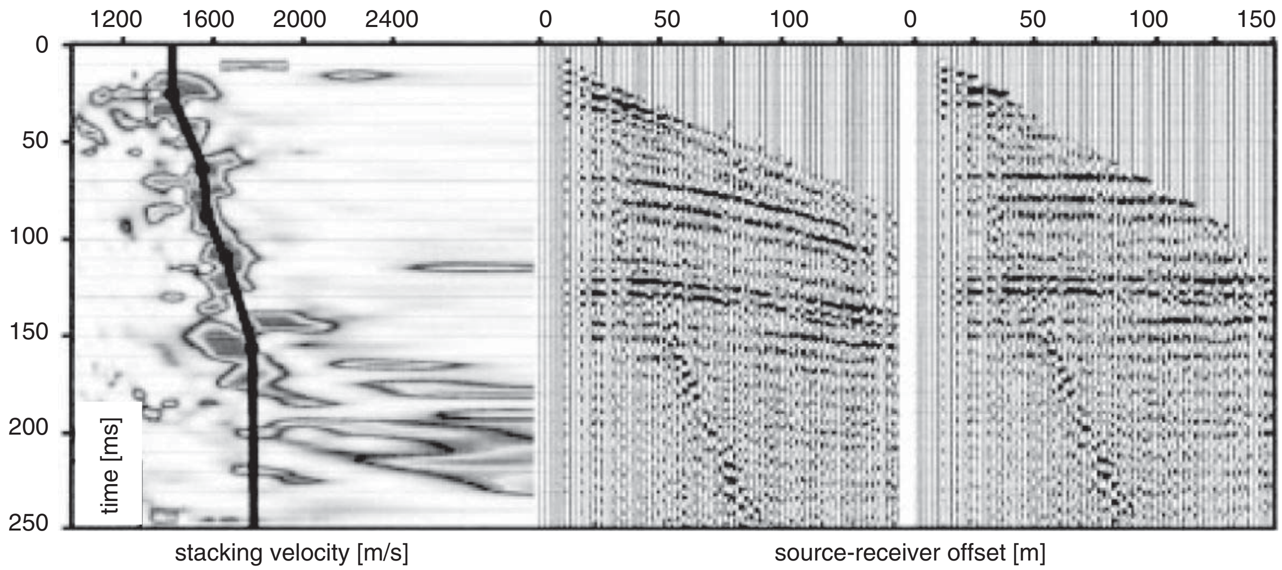

Figure 6.33 (Left) Determination of stacking velocity by passing a continuous curve through regions of high (red) values of semblance; (middle) an uncorrected CMP supergather; (right) the NMO-corrected CMP supergather using the stacking-velocity function in the left panel. After Spitzer *et al*. (2003).

similarity between a large number of trial hyperbolas and the actual hyperbolas present on a CMP (super)gather. A semblance contour plot is constructed with the trial stacking velocity on the horizontal axis and the zero-offset time, or equivalently an apparent depth, on the vertical axis. The best stacking velocity, for a given apparent depth, corresponds to the highest value of the semblance. An example of a semblance-based velocity analysis of a CMP supergather appears in Figure 6.33. The stacking velocity curve (solid line, left panel) is chosen as one that joins regions of high semblance values. Using this velocity function in the NMO process tends to flatten out the hyperbolic reflection events seen in the CMP supergather (middle and right panels).

Linear τ–p filtering. Another means of separating primary reflection events from other types of source-generated energy such as surface waves, refractions, direct waves, and guided waves is via a linear *τ–p transformation*. The essential mathematics of the transformation (Diebold and Stoffa, 1981) is summarized in Appendix C for a simple three-layer case without dip. As shown in the appendix, transforming a shot gather from the familiar *t–x* domain into the linear *τ–p* domain converts events that have linear moveouts, such as direct, guided, and surface waves, into points. Hyperbolic reflecting events in the *t–x* domain are mapped into elliptical-shaped curves in the linear *τ–p* domain. This property facilitates the separation of wanted reflected signals from the remaining source-generated energy, which in reflection imaging is regarded as noise. After filtering, an inverse *τ–p* transformation is performed to reconstruct the original shot gather in the *t–x* domain, without the source-generated noise.

A linear *τ–p* transformation of a synthetic shot gather is illustrated in Figure 6.34a, from a paper by Spitzer *et al*. (2001). The synthetic data are generated from a four-layer velocity model by a finite-difference simulation and are plotted for convenience using the reduced

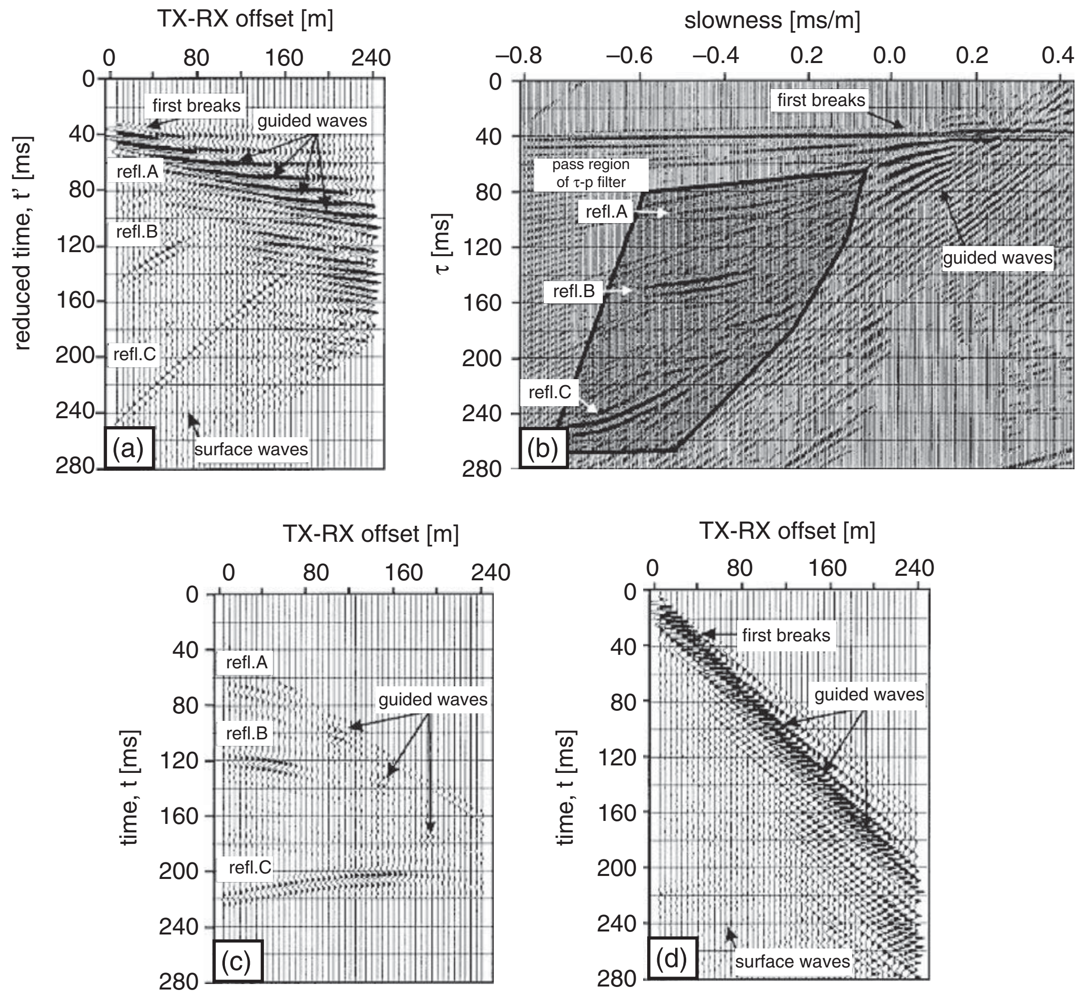

Figure 6.34 The results of linear τ–p processing on synthetic data: (a) finite-difference simulated shot gather plotted using reduced traveltime; (b) result of linear τ–p transformation; the black line outlines the pass region; (c) result of the inverse linear τ–p transformation after filtering; (d) the source-generated noise removed by the linear τ–p processing. After Spitzer *et al.* (2001).

traveltime $t' = t + 30 - x/1700$ [ms]. The velocity model contains a dipping reflector. Moreover, near-surface waveguiding effects and surface waves are included in the simulation. The results of the linear τ–p transformation are shown in Figure 6.34b. The black line outlines the pass region of the τ–p filter. The pass region is selected as one which contains mainly the elliptic-shaped curves characteristic of reflection events (see Appendix C). The results of the inverse linear τ–p transformation are shown in Figure 6.34c. Note that the energy from model reflectors A, B, and C is enhanced. The source-generated noise that was removed using this procedure is shown in Figure 6.34d.

Migration. As described already, CMP stacking of NMO-corrected traces assume that all energy originates from a single point on a subhorizontal reflecting horizon located directly beneath the TX–RX midpoint. This assumption is not correct in the presence of dipping reflectors or in the case of diffractions from edges. The purpose of *migration* is to image

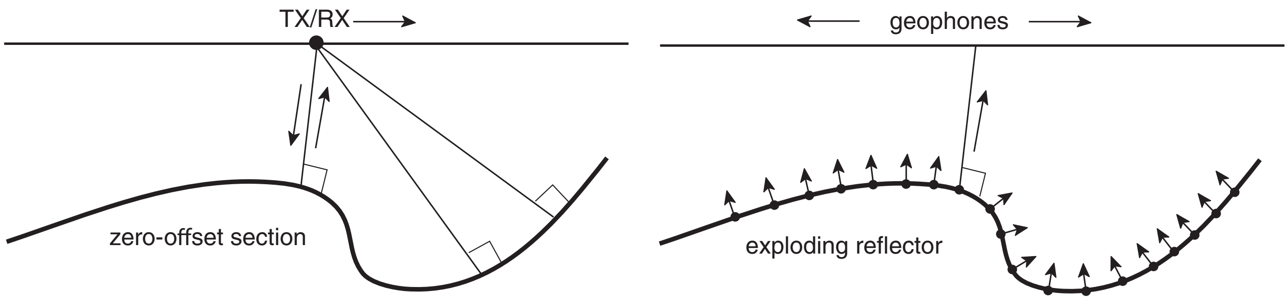

Figure 6.35 The exploding-reflector concept. Adapted from material on the Stanford Exploration Project website, sepwww.stanford.edu.

subsurface dipping reflectors and diffracting points at their correct positions within the subsurface, essentially undoing the effects of wave propagation. Over the past decade, sophisticated algorithms have emerged for migrating seismic data on exploration length scales (Etgen *et al*., 2009). An excellent survey of the development of migration from its historical roots to its modern application in the oil and gas sector is given in Gray *et al*. (2001).

Migration can be applied either before or after the CMP stack. A small number of near-surface geophysicists have applied DMO/pre-stack migration and some have investigated post-stack migration. It has been found, however, that data quality must be very high for migration to be successful. Especially in the uppermost several tens of meters, strong velocity contrasts and heterogeneities are present, leading to severe static effects and dominant source-generated noise. Migration in this case can introduce significant artifacts and can actually degrade a geological interpretation; thus migration is not always used for very shallow applications. For seismic acquisition layouts that probe to greater depths, in the range of ~ 200–500 m, data quality is typically better such that pre-stack migration is often effective (G. Baker, personal communication.)

There are two types of migration: reverse-time and depth migration. Reverse-time migration does not attempt to develop a geologically reasonable subsurface velocity model; rather it uses an ad hoc velocity function that produces a pleasing image containing coherent reflections. Depth migration is more involved as it first tries to estimate and then utilize an accurate model of the subsurface velocity distribution. In areas of structural complexity, however, the velocity distribution can be very difficult to determine. There are many different migration procedures used in geophysics. A detailed exposition of the various possibilities is beyond the scope of the book but I can refer the reader to Etgen *et al*. (2009). Herein, only the elementary *reverse-time Kirchhoff* method is discussed. The discussion is drawn largely from a tutorial on the Stanford Exploration Project website, sepwww.stanford.edu.

Consider the seismic experiment portrayed in Figure 6.35, left, in which seismic energy propagates downward and outward from a source (TX), reflects from a subsurface horizon, and then propagates upward to a co-located receiver (RX). Notice in this scenario that three primary reflection events will be recorded; these are shown on the illustration. The multiplicity of reflected arrivals is a consequence of the undulations in the reflecting horizon. Now suppose the co-located TX–RX pair is moved along the acquistion surface,

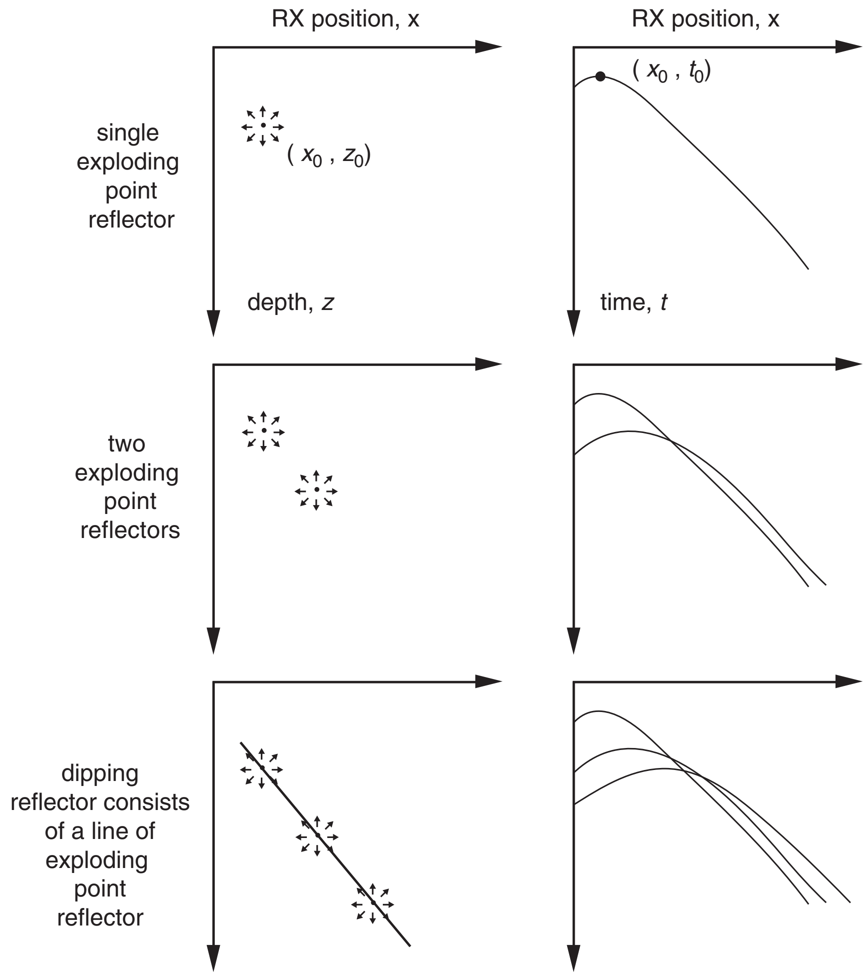

Figure 6.36 Forward modeling using the exploding-reflector concept.

as shown. A zero-offset time section can be constructed. However, the undulating horizon would not be correctly imaged in the section since, as we have already seen, the single horizon produces multiple reflection events.

Figure 6.35, right, is a schematic illustration of the *exploding-reflector* concept attributed to Loewenthal *et al*. (1976). The main idea is that we would get exactly the same zero-offset time section if, instead of moving the single TX–RX pair along the profile, each point on the subsurface horizon were somehow to simultaneously explode and we could record the resulting signals with a geophone array spread across the surface. The observed wavefields $u(x, t)$ in the two experiments, the actual one at left and the hypothetical one at right, would be identical (with the exception that the traveltimes in the hypothetical experiment are just one-half those of the actual experiment). The exploding-reflector concept is simple yet powerful. In fact, the reader should be able to judge the validity of the exploding-reflector concept by thinking about Huygens principle, which states that each point on a reflecting wavefront acts as a spherically spreading point source.

Figure 6.36 illustrates how the exploding-reflector concept can be used to predict the wavefield due to reflections from an undulating horizon. At top left is shown a single

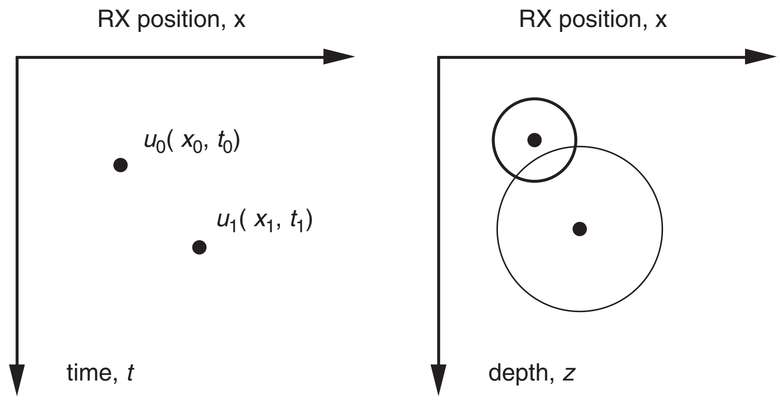

Figure 6.37 Kirchhoff imaging principle.

exploding point reflector at some location (x_0, z_0) in the subsurface. This explosion acts as a point source of spherically expanding seismic energy. An analysis of the normal moveout of this energy reveals that it should appear to a surface geophone array as a diffraction hyperbola with its apex at (x_0, t_0), as shown at top right. The transformation from depth to time is given by the familiar hyperbolic equation

$$V^2t^2 = (x - x_0)^2 + z_0^2. \tag{6.50}$$

The middle panels show the corresponding situation for two exploding point reflectors, in which case two diffraction hyperbolas should be observed by the geophone array. It should now be clear that a dipping reflecting horizon can be modeled as a continuous line of exploding point reflectors. Three of these explosions are shown for simplicity at bottom left. The dipping reflecting horizon appears on the geophone array as the superposition of many diffraction hyperbolas; again, just three of these are shown at bottom right. This example shows how the exploding-reflector concept can be used to predict the wavefield generated by seismic excitation of a physical Earth structure. The next task is to consider the reverse process, namely, how to construct an image of the physical Earth structure based on an observed seismic wavefield.

Figure 6.37 describes the key aspect of the Kirchhoff imaging principle. We work in two dimensions for simplicity although the generalization to three dimensions is straightforward. At left are shown two samples of an observed seismic wavefield $u(x, t)$. At right, these two data points are transformed from time t into depth z using the transformation (6.50). The seismic energy u_0 that is observed at location (x_0, z_0) could have arrived there from any point or points on a circle of radius Vt_0, where V is the velocity of the medium; similar remarks apply for the energy u_1 at location (x_1, z_1). We therefore construct two circular mirrors, as shown: a smaller one of radius Vt_0 centered on (x_0, z_0) that has strength, or reflectivity, u_0; and a larger one of radius Vt_1 centered on (x_1, z_1) that has strength, or reflectivity, u_1. We construct a similar circular mirror for each data sample in the wavefield. Then, we simply add all the circles together to produce the Kirchhoff image.

To understand how Krichhoff imaging works, consider the following. Suppose the seismic energy observed at $u_0(x_0, t_0)$ and $u_1(x_1, t_1)$ originated from just a single exploding reflector. That reflector must be located at one of the two intersection points of the circles.

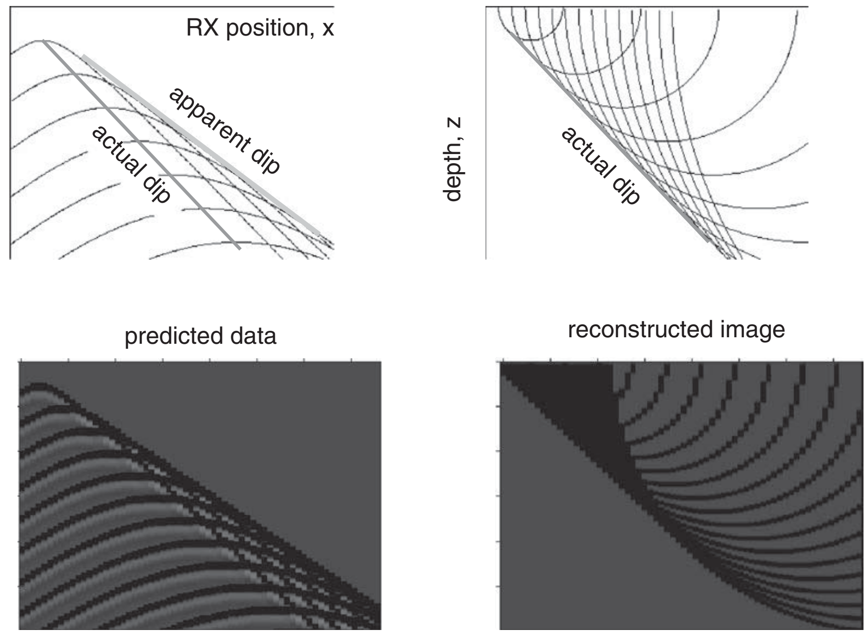

Figure 6.38 Kirchhoff reverse-time imaging of a dipping reflector. Adapted from material on the Stanford Exploration Project website, sepwww.stanford.edu.

Adding the two circles together produces the largest amplitudes at the intersection points. In other words, the two possible locations of the reflector contribute most to the summation. A more detailed imaging example is shown in Figure 6.38. The left panels show, using two different display formats, the modeled wavefield due to a dipping reflector (compare to Figure 6.36, bottom right). This wavefield has again been computed based on the exploding-reflector concept. Notice that the dip of the reflector is not correct. The apparent dip is shallower than the actual dip. At right are shown the Kirchhoff circular mirrors. The reconstructed image is the superposition of the circular mirrors. Notice that the greatest amplitudes in the image are found, as desired, along the actual dip of the reflector.

3-D example. An example of a complete suite of 3-D seismic-reflection data-processing steps is given by Kaiser *et al*. (2011). This study of an active, oblique-slip segment of the Alpine fault zone in New Zealand is one of the first published reports on a 3-D near-surface seismic survey. While a 3-D dataset is clearly more time-consuming to acquire and process than a 2-D counterpart, a 3-D survey permits better imaging of complex fault geometries, including out-of-plane reflectors and diffractors. The acquisition layout in the New Zealand survey included 24 parallel source lines and 27 parallel receiver lines, each of ~ 500 m length, running perpendicular to the fault strike. The source spacing was 8 m and the receiver spacing was 4 m, which resulted in an average fold of ~ 20. The line spacing was ~ 10 m. Due to cost and time constraints, most of the TX–RX pairs however were nearly in-line, resulting in a limited azimuthal coverage. Ideally, a 3-D seismic survey would consist of full, densely sampled TX–RX azimuthal coverage.

Pre-stack processing steps included deconvolution, mutes, static corrections, τ–p filtering, velocity analysis on CMP supergathers, and NMO and DMO corrections. The

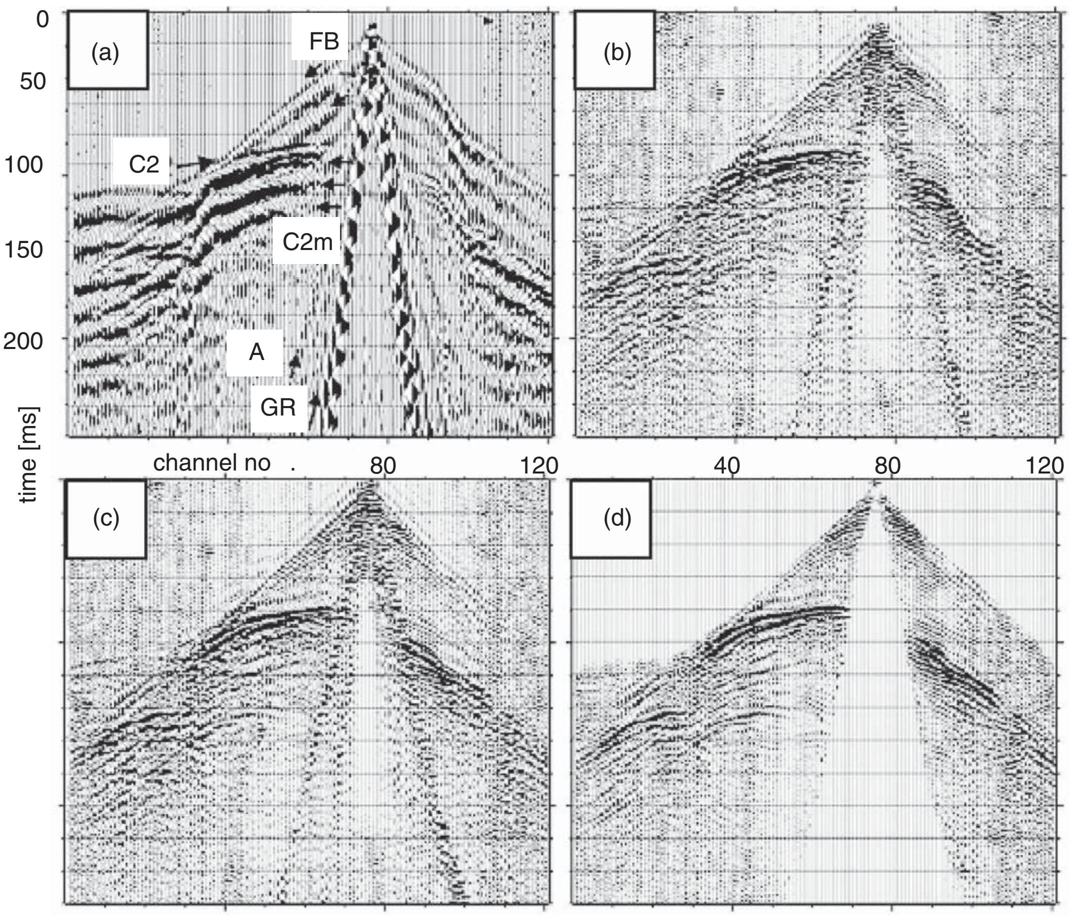

Figure 6.39 Effects of pre-stack processing steps on a high-resolution shot gather from an Alpine fault zone, New Zealand; A = air wave, GR = ground roll, FB = first breaks, C2 = basement reflection, C2M = basement reflection multiples; (a) raw shot gather with automatic gain control (AGC) applied; (b) deconvolution and bandpass filter applied; (c) static (refraction and residual) corrections applied; (d) mutes and τ–p filtering applied; after Kaiser *et al*. (2011).

effects of some of the pre-stack processing steps on a typical shot gather are shown in Figure 6.39. It is easily seen in the figure that the result of the pre-stack processing provides a better definition of the near-surface reflections, along with suppression of source-generated noise.

The post-stack processing included bandpass filtering, followed by 3-D depth migration. The migration algorithm collapsed most of the diffractions that were evident on the unmigrated sections. The interpreted main fault strand (AF) dipping at ~ 80°, along with a subsidiary fault strand (SF), are indicated by the dotted lines in the migrated 2-D section at Figure 6.40, left. The strong reflecting events C1 and C2 are from, respectively, the footwall and the hanging wall of the fault in late-Pleistocene basement. The borehole intersects the basement at ~ 26–30 m depth, in agreement with the location of the basement seismic reflector. The A and B reflectors are due to stratification within the overlying glaciolacustrine and glaciofluvial sediments. The migrated full 3-D volume is shown in

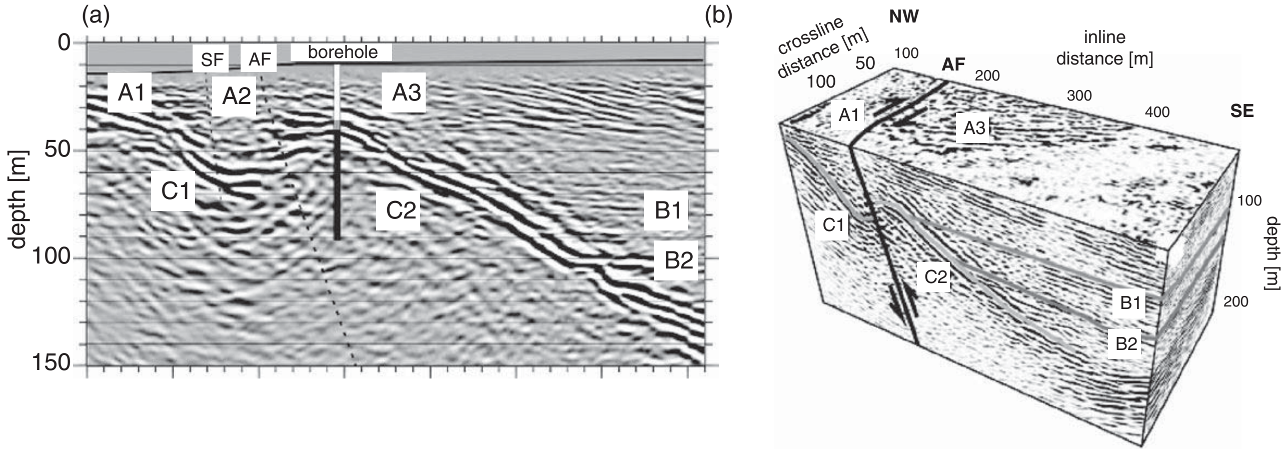

Figure 6.40 High-resolution near-surface reflection data from the Alpine fault zone, New Zealand: (a) a migrated 2-D section extracted from the migrated 3-D volume shown in (b); after Kaiser *et al*. (2011).

(Figure 6.40, right) in which it can be seen that the fault zone is imaged continuously along the strike of the main strand.

6.16 Ray-path modeling

The propagation of seismic waves though heterogeneous elastic media, possibly containing acoustic impedance discontinuities, can be approximated by *ray tracing*. By analogy with geometric optics, seismic wavefront tracking in the high-frequency approximation is described by rays. A ray is a narrow, pencil-like beam that reflects and refracts at material interfaces and bends as it travels in materials characterized by a continuously varying velocity structure. The ray approximation is excellent if the seismic wavelength is small in comparison to the characteristic length-scale of the material heterogeneities. Ray tracing constitutes the forward modeling component of many popular seismic tomographic reconstruction algorithms (e.g. Zelt *et al*, 2006).

Here we provide the classical derivation of ray trajectories $x(t)$ and $z(t)$ in a 2-D acoustic medium (Eliseevnin, 1965). The acoustic wave equation is

$$\frac{\partial^2 p}{\partial x^2} + \frac{\partial^2 p}{\partial z^2} = \frac{1}{c^2}\frac{\partial^2 p}{\partial t^2}, \tag{6.51}$$

where $c(x, z)$ is the acoustic wave speed and p is the pressure field. An acoustic medium can support compressional but not shear waves. Assume that the pressure field is time harmonic, $p(x, z, t) \sim \exp(-i\omega t)$. We can expand the pressure field into a power series in inverse powers of frequency,

$$p(x,z) = \exp(-i\omega\tau)\sum_{n=0}^{\infty}\frac{u_n}{(i\omega)^n} \tag{6.52}$$

for which $\tau(x, z)$ is a traveltime, or *pseudophase*, function and $u_n(x, z)$ is an amplitude function.

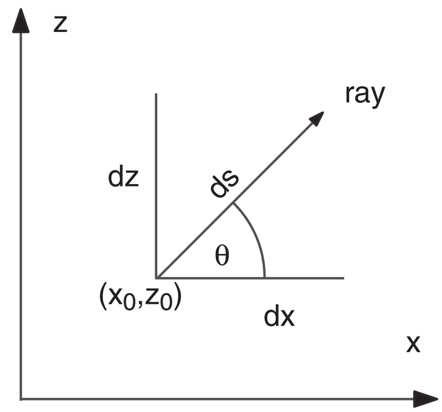

Figure 6.41 A ray emanating from point (x_0, z_0).

The series is rapidly convergent for the high frequencies at which the ray approximation is valid. Inserting Equation (6.52) into (6.51) and keeping the highest-order terms results in the *eikonal equation*

$$\left(\frac{\partial\tau}{\partial x}\right)^2 + \left(\frac{\partial\tau}{\partial z}\right)^2 - n^2 = 0, \tag{6.53}$$

where $n^2 = 1/c^2$ is the squared wave slowness function.

The eikonal equation describes the spatial distribution of the traveltime $\tau(x, z)$ function in a medium characterized by acoustic wavespeed $c(x, z)$. The interpretation of the traveltime function is that, for any location (x, z) within the medium, the first wave arrives at time $t = \tau$. Hence, solving the eikonal equation provides a method for predicting the first-arriving waveform at any location throughout the medium. To see how the ray trajectories $x(t)$ and $z(t)$ are related to the eikonal equation, consider the ray shown in Figure 6.41. Let s be the distance along the ray such that $c(x, z) = ds/dt$.

From the figure, we can see that $dx = ds \cos \theta$ and $dz = ds \sin \theta$. Then it follows that

$$\frac{dx}{dt} = \cos\theta \frac{ds}{dt} = c\,(x, z)\cos\theta; \tag{6.54a}$$

$$\frac{dz}{dt} = \sin\theta \frac{ds}{dt} = c\,(x, z)\sin\theta. \tag{6.54b}$$

We can use Equations (6.54a, b) to propagate the ray forward from point (x_0, z_0) if we know the angle θ. Once the ray arrives as the new point (x_1, z_1) we need to know the new ray direction θ. To find an equation for $d\theta/dt$, the eikonal equation (6.53) is re-written as

$$\frac{1}{n^2}\left(\frac{\partial\tau}{\partial x}\right)^2 + \frac{1}{n^2}\left(\frac{\partial\tau}{\partial z}\right)^2 = 1 = \cos^2\theta + \sin^2\theta, \tag{6.55}$$

from which we can identify $\cos\theta = (1/n)\,\partial\tau/\partial x$ and $\sin\theta = (1/n)\,\partial\tau/\partial z$. After some algebra, the details of which can be found in Eliseevnin (1965), the following equation is obtained:

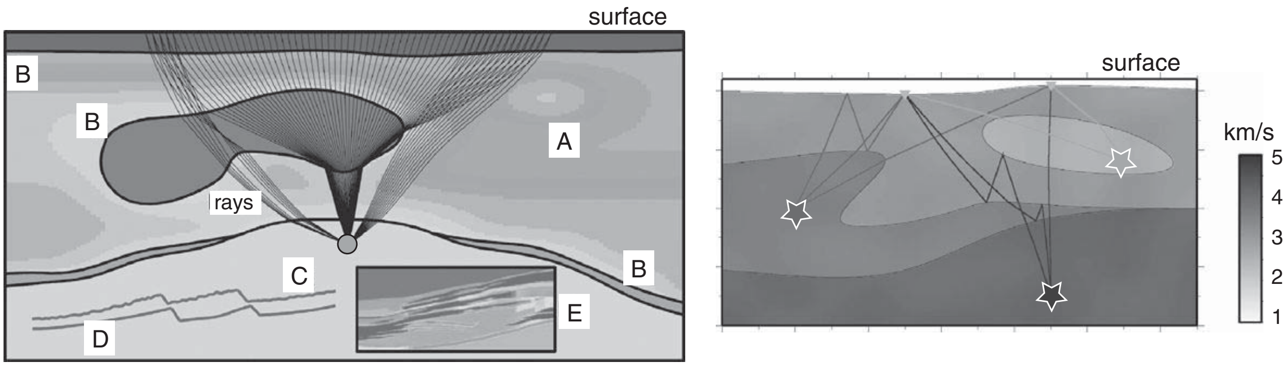

Figure 6.42 (Left) Rays traced from a subsurface source (green dot) through a complex-shaped fast-velocity anomaly to the surface (after Gjoystdal *et al*. 2007). (Right) Different ray paths are possible in complicated models, such as this one containing a pinchout, overturned fold, and anomalously fast body (after Hauser *et a*l., 2008).

$$\frac{d\theta}{dt} = \frac{\partial c}{\partial x}\sin\theta - \frac{\partial c}{\partial z}\cos\theta\,. \tag{6.56}$$

Together, Equations (6.54) and (6.56) represent a system of ordinary differential equations whose solutions determine ray paths through an inhomogeneous acoustic medium. A ray-tracing algorithm simply integrates this system of equations through time from $t = 0$ and a given source location (x_0, z_0). The geometry of a ray path is heavily influenced by the initial take-off angle θ_0.

In areas of structural complexity, iterative ray tracing can be used to determine a seismic velocity model that is consistent with the seismic observations. The typical assumption is that reflections mark boundaries between undulating layers of uniform velocity. The essential rule is that the rays obey Snell's law at each interface. Some examples of ray tracing in complex geology are shown in Figure 6.42. Information about the subsurface is obtained only for those regions that are illuminated by rays. Note that, for each of the three subsurface sources shown in Figure 6.42 right, rays that emanate with slightly different take-off angles can follow very different pathways and provide information about very different structures within the model.

In Figure 6.43, it is shown how ray tracing can be used to understand complex wavefront morphologies, such as a *triplication*, which can develop even for relatively simple structures such as a slow anomaly embedded in a faster host medium. The convoluted shape of the wavefront at time $t + \Delta t$ may also be understood by applying Huygen's principle to the wavefront at time t. The three arc segments labeled 1, 2, and 3 comprising the triplication form a characteristic "bowtie" structure. The inset in the figure shows that the signal at the receiver contains three distinct arrivals corresponding to the three ray paths. The first arrival is via ray path 1, which has traversed only the faster host medium. The second and third arrivals are via ray paths 2 and 3, respectively, which have traversed the slower anomalous zone.

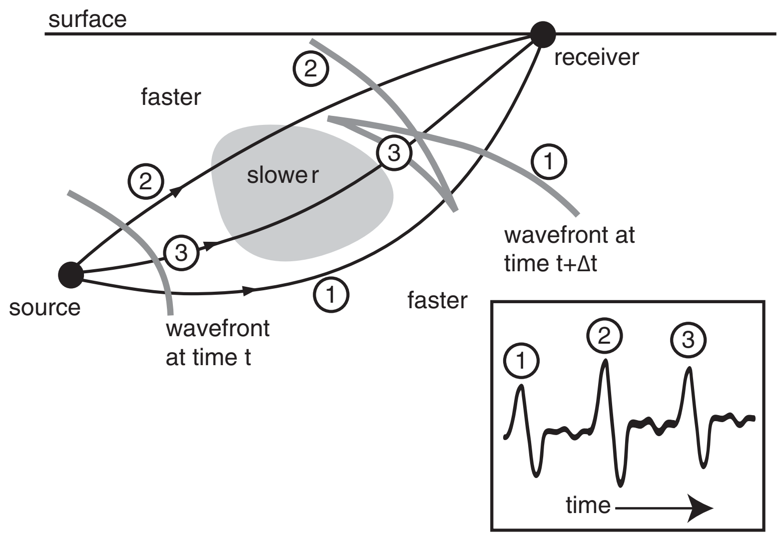

Figure 6.43 Ray paths for a medium containing a slow velocity anomaly showing a triplication. The bottom, top, and middle rays are respectively the first, second and third arrivals at the receiver. After *Hauser et al*. (2008).

6.17 Illustrated case studies

The following two case studies illustrate recent developments of the seismic-reflection and -refraction techniques for near-surface investigation.

Example. 3-D refraction tomography at a contaminated site.

A 3-D seismic-refraction survey at a Superfund site within Hill Air Force Base in Utah is described by Zelt *et al*. (2006). A long history at this location of using chlorinated solvents as an industrial cleansing agent has led to the infiltration of DNAPL contaminants below ground surface and their pooling at the base of a surficial sand and gravel aquifer of 2–15 m thickness. The water table is at 9–10 m depth. The refraction survey objective was to image, over an area of ~ 0.4 ha, a paleochannel incised into the top surface of an impermeable silty clay layer that underlies the aquifer. A static array of 601 40-Hz geophones connected to data loggers sampling at 1 ms was laid out in 46 parallel lines, each containing either 13 or 14 geophones, with 2.1-m line spacing and 2.8-m station spacing. A total of 596 shots were deployed using a .22-caliber rifle, with each shotpoint nominally located, where possible, within 0.3 m of a geophone. The maximum TX–RX offset distance is 102 m. The resulting shot gathers were minimally filtered using a bandpass filter to remove ground roll and a 60/120-Hz notch filter to remove cultural electrical noise caused by routine base activities. A few of the first-arrival picks, and the survey geometry, were shown earlier in Figure 6.26.

The 3-D regularized tomographic algorithm described by Zelt and Barton (1998) was used to convert the observed first-arrival traveltimes into a subsurface velocity model. The algorithm, which uses ray tracing as the forward module, favors subsurface models which

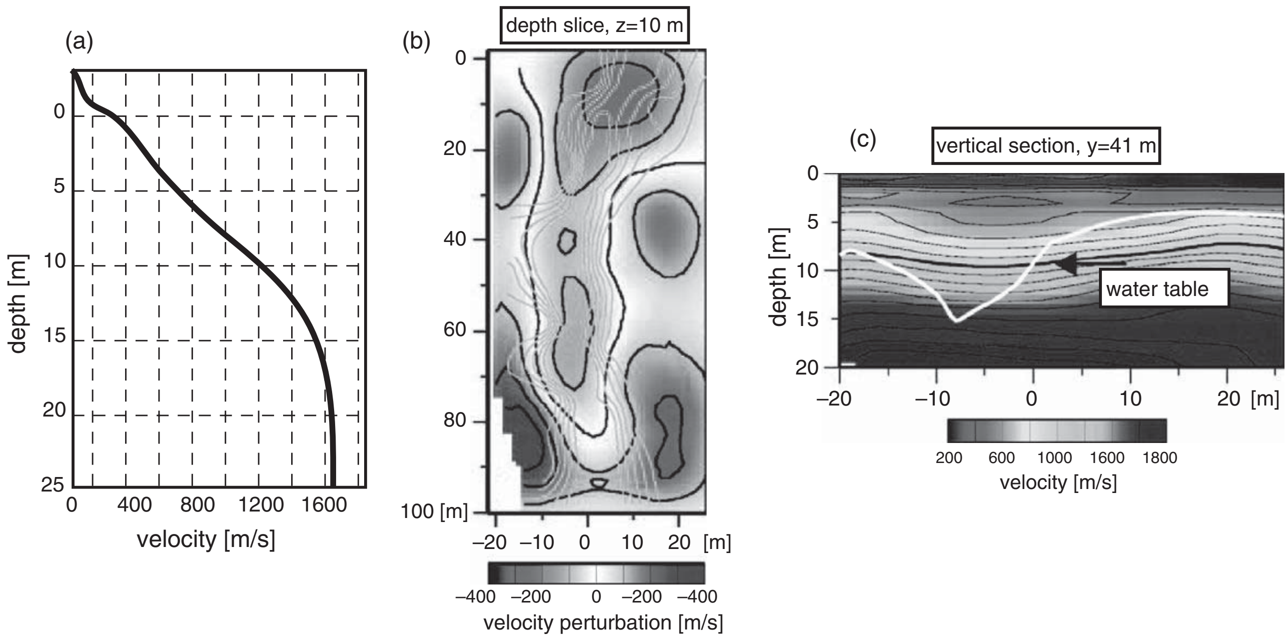

Figure 6.44 3-D refraction tomography at a contaminated site: (a) starting 1-D velocity model; (b) horizontal slice at depth $z = 10$ m through the final preferred tomogram; (c) vertical slice at location $y = 41$ m; green and white contours mark the incised paleochannel inferred from well data. After Zelt *et al*. (2006).

contain smooth spatial variations in the velocity structure; i.e. spatially rough velocity models are suppressed. A discussion of tomographic methods and their regularization appears later in this book in Chapter 12. The starting 1-D velocity model, along with horizontal and vertical slices through the preferred final 3-D tomogram, are shown in Figure 6.44. It is easily seen that a low-velocity zone outlines the shape of the incised paleochannel inferred from drilling and well data. This case study demonstrates both the feasibility and utility of tomographic reconstruction of the near-surface 3-D seismic velocity distribution beneath a contaminated site located at an active military-industrial facility.

Example. Reflection imaging of a buried subglacial valley.

Buried subglacial valleys that form as continental ice sheets retreat are interesting geophysical targets since they often do not have a distinctive geomorphological signature, they provide a record of climate history, and they can host valuable resources such as groundwater, sand and gravel aggregates, and methane gas. Ahmad *et al*. (2009) describe a high-resolution seismic-reflection survey conducted over a subglacial valley in northwestern Alberta, Canada to determine its architecture and to study the hydrological and mechanical processes beneath retreating ice sheets.

The study area is covered by Quaternary glacial deposits left in the wake of Wisconsin glaciation ~ 10 ka. The underlying bedrock is Cretaceous shales ~ 100 Ma, beneath which

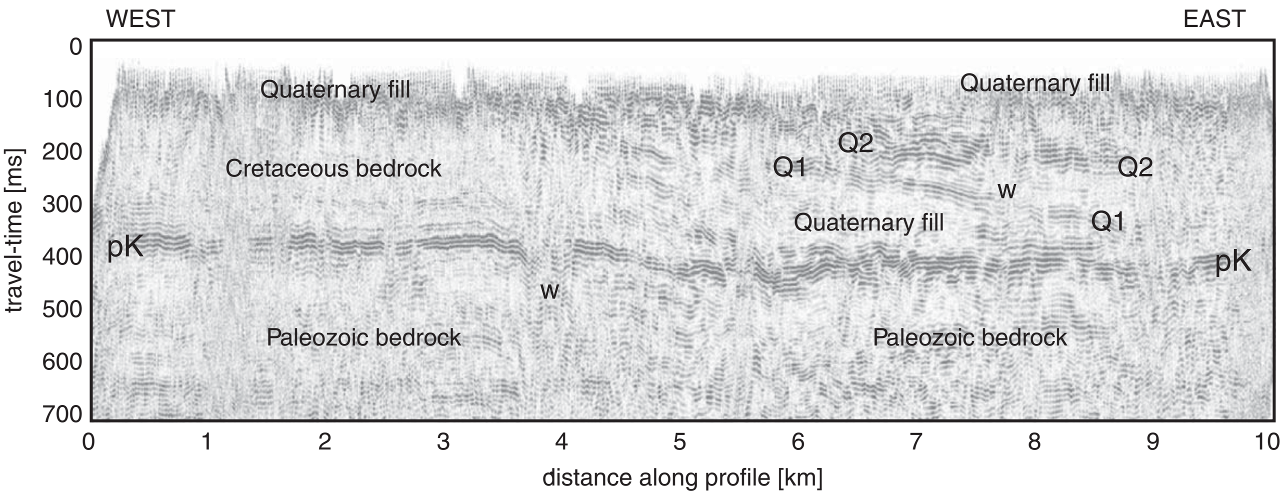

Figure 6.45 Seismic-reflection profile from a buried subglacial valley, Alberta, Canada. See text for details. After Ahmad *et al*. (2009).

are Paleozoic carbonates ~ 340 Ma. The presumably steep-walled valley is filled with ~ 300-m drift, mainly stratified tills and coarse-grained glaciofluvial and glaciolacustrine sediments. A previously known geophysical log intersected a shallow, high-resistivity (30–100 Ω m) gas-bearing zone at 64–72-m depth.

The objective of the reflection survey was to image the uppermost ~ 350 m. Acquisition parameters included 4-m geophone spacing and 24-m shotpoint spacing along a 10-km profile using a source consisting of a vibrator swept in frequency from 20–250 Hz and a 240-channel seismograph. A standard CMP data processing sequence was used with average fold ~ 40. Strong near-surface lateral heterogeneity due to muskeg caused troublesome statics that affected the traveltimes to deeper reflectors. Stacking velocities were determined using a semblance-based velocity analysis. Higher velocities were found to the west that indicated the presence of a thick Cretaceous sequence there. Seismic-refraction analysis and a co-located electrical resistivity tomography (ERT) profile strongly supported this inference.

The final processed reflection profile is shown in Figure 6.45. It shows some washed-out zones marked "w" that extend vertically through the section. These do not contain any reflections and could be associated with free gas saturation. The Cretaceous–Paleozoic unconformity marked "pK" at ~ 300 m depth is the most conspicuous reflecting horizon; it is present all along the profile except in the washout zones. The pK reflection horizon appears to undulate but this could be caused by lateral velocity variations in the overlying zones. Lower velocities occur toward the east, associated with thickening of the low-velocity Quaternary fill and the absence of Cretaceous strata. These low velocities tend also to "pull down" the pK reflector. The reflection data poorly image the putative steep valley wall (suggested by the refraction and ERT data) at ~ 3–4 km along the profile. There are some reflectors contained within the Quaternary fill marked as "Q1" and "Q2". There is some concern that these might be multiply reflected events but generally they indicate internal stratification within the Quaternary fill layer.

Problems

1. Show that the law of reflection and Snell's law of refraction may be derived from Fermat's principle of least time, which states that the ray path from a seismic source to a seismic receiver is the one that minimizes the traveltime along the path.
2. Assuming that the TX–RX offset distance x is much less than the layer thickness h, which of course is not always a good assumption in near-surface geophysics, show that the NMO correction is approximately $\Delta T(x) \sim x^2/2T_0V_1^2$.
3. Consider a reflection seismic experiment that includes both diffraction from an edge and multiple reflections. Show that the diffraction hyperbola and the multiple reflections do not align horizontally if an NMO correction based on the primary reflection is applied to each trace. Use the same $x << h$ approximation as in the previous exercise.
4. Assume that the velocity V is known in a reflection experiment over a dipping interface. Derive expressions for down-dip and up-dip traveltimes τ_D and τ_U based on a single source location and a single (moveable) geophone. How might the dip angle φ and depth to the interface h be derived from the two traveltime measurements, assuming that the dip angle φ is small enough that the depth h to the interface is approximately the same for both the up-dip shot and the down-dip shot. What additional measurement, apart from the direct-wave traveltime, should be made if the velocity V is also to be determined?
5. Show that the seismic-refraction cross-over distance x_C, beyond which the head wave arrives earlier than the direct wave, is given by the formula

$$x_C = 2h\sqrt{(V_2 + V_1)/(V_2 - V_1)}.$$

6. Consider a down-dip refraction experiment. (a) Show that the head-wave traveltime curve $T_D(x)$ is given by Equation (6.39), which implies that the down-dip refracted wave moves out with apparent velocity $V_D = V_1/\sin(i_C + \varphi)$. (b) Using a similar analysis, show that the apparent up-dip velocity is $V_U = V_1/\sin(i_C - \varphi)$. (c) Show that the dip angle is given by Equation (6.40).
7. Consider a short pulse consisting of the superposition of two equal-amplitude sinusoidal waves each of the form $\exp[i(\omega t - \beta x)]$ and oscillating at closely spaced frequencies $\omega \pm \Delta\omega/2$ and wavenumbers $\beta \pm \Delta\beta/2$. Show that the pulse consists of *beats*, which move with a group velocity v_g that is related to the phase velocity v_p of the individual sinusoids by $v_g = v_p + \beta dv_p/d\beta$.
8. Show that the bulk modulus, for an elastic body under hydrostatic pressure, is the ratio of the pressure p to the dilatation Δ.
9. Derive Equation (6.7a) starting from Equation (6.6).
10. Show that the refraction traveltime curve $t_2(x)$ for propagation through a two-layer Earth is given by the equation

$$t_2(x) = \frac{x}{V_3} + \frac{2h_2}{V_2}\cos\theta_{C2} + \frac{2h_1}{V_1}\cos\theta_{C1},$$

where the upper layer is characterized by thickness and velocity (h_1, V_1), the underlying layer by (h_2, V_2) and the terminating halfspace by velocity V_3. This equation is the form of a straight-line segment with slope $1/V_3$ and intercept given by the sum of the last two terms.

11. Derive the eikonal Equation (6.53).